

THESIS FOR THE DEGREE OF LICENTIATE OF ENGINEERING

Microstructural development in laser-based powder bed fusion
- from ferritic stainless steel to medium entropy alloys

SRI BALA ADITYA MALLADI



CHALMERS
UNIVERSITY OF TECHNOLOGY

Department of Industrial and Materials Science
CHALMERS UNIVERSITY OF TECHNOLOGY
Gothenburg, Sweden, 2021

Microstructural development in laser-based powder bed fusion
- from ferritic steels to medium entropy alloys

SRI BALA ADITYA MALLADI

© SRI BALA ADITYA MALLADI, 2021

Technical report no IMS-2021-22

Licentiate Thesis at Chalmers University of Technology

Department of Industrial and Materials Science

Chalmers University of Technology

SE-412 96 Gothenburg

Sweden

Tel: +46 (0)31 772 1000

Printed by Chalmers Reproservice

Gothenburg, Sweden 2021

विद्यानाम नरस्य रूपमधिकं प्रच्छन्न गुप्तं धनं
विद्या भोगकरी यशस्सुखकरी, विद्या गुरूणां गुरुः।
विद्या बन्धुजनो विदेशगमने विद्या परादेवता
विद्या राज्य सुपूजिता नहि धनं, विद्या विहीनः पशुः।।

Microstructural development in laser-based powder bed fusion

- *from ferritic steels to medium entropy alloys*

Sri Bala Aditya Malladi

Department of Industrial and Materials Science
Chalmers University of Technology

Abstract

Ever since the advent of additive manufacturing (AM), the interest in AM technologies has skyrocketed due to its intrinsic ability to produce near net shaped components. Laser-based powder bed fusion (LB-PBF), being one of the most widely adapted AM technologies, has been especially a game changer due to its ability to produce components of complex geometries with improved designs and to reduce not only the final weight of the products but also the amount of the waste produced. However, the rapid melting and solidification in the LB-PBF process usually result in anisotropy in properties with respect to different printing directions, due to the epitaxial growth of columnar grains. One way to address this issue is by developing the alloy systems tailored to the LB-PBF process conditions, thereby achieving more control over the solidification dynamics to produce parts with more isotropic properties.

One possible solution to inhibit the columnar growth of grains is by inducing in-situ inoculation via alloy design, thereby reducing the undercooling required for the growth of columnar grains. The first part of this work focuses on *in-situ* inoculation for ferritic stainless steels via alloy design to achieve the columnar to equiaxed transition. Three different ferritic steel grades based on SS441 were studied, with the aim of exploring the effectiveness of TiN as an inoculant in the LB-PBF process. The results showed that a substantial reduction in grain size with concomitant changes in the solidification behaviour occurred in the alloys pre-alloyed with inoculant forming elements, compared to the alloy without those inoculant forming elements.

The second part of this thesis explores the possibility of improving the strength of the equiatomic CoCrNi medium entropy alloys by the addition of nitrogen. The motivation is to take advantage of the rapid melting and solidification that are intrinsic to the LB-PBF process and to stabilize nitrogen as an interstitial solid solution strengthening element. Two different grades of CoCrNi, one without nitrogen and one pre-alloyed with nitrogen, have been studied. Printing with optimized parameters resulted in parts with densities greater than 99.9% with cellular solidification structure. Heat treatments of printed CoCrNi specimens resulted in the nucleation of chromium rich oxides, while no nitrogen rich phases were observed. The expected interstitial solid solution strengthening resulted in improved yield and ultimate tensile strength values from about ~730 and ~970 MPa to ~890 and ~1110 MPa, respectively.

Keywords: Laser-based powder bed fusion, inoculation, ferritic stainless steels, medium entropy alloys, interstitial solid solution strengthening, microstructural characterization, mechanical properties.

PREFACE

This licentiate thesis is based on the work performed in the Department of Industrial and Materials Science at Chalmers University of Technology from June 2019 to October 2021. The work has been carried out under the supervision of Professor Lars Nyborg and Professor Sheng Guo. This work has been performed within the framework of project funding from strategic innovation program Metalliska Material through the project Design of novel materials and processes for next generation additive manufacturing (DEMA), financed by the Swedish Governmental Agency for Innovation Systems (VINNOVA) and Centre for Additive Manufacture-Metal (CAM²).

This thesis consists of an introductory part with an emphasis on aspects related to microstructural development during additive manufacturing and a summary of results, which is included in the following appended papers.

List of appended papers

- Paper I: Grain refinement in additively manufactured ferritic stainless steel by *in situ* inoculation using pre-alloyed powder**
A. Durga, Niklas Holländer Pettersson, Sri Bala Aditya Malladi, Zhuoer Chen, Sheng Guo, Lars Nyborg, Greta Lindwall, Scripta Materialia, Vol. 194, 2021, 113690, DOI: [10.1016/j.scriptamat.2020.113690](https://doi.org/10.1016/j.scriptamat.2020.113690).
- Paper II: Influence of in-situ inoculation on microstructure of ferritic stainless steel manufactured by laser-based powder bed fusion**
Sri Bala Aditya Malladi, Zhuoer Chen, A. Durga, Greta Lindwall, Sheng Guo, Lars Nyborg
In manuscript
- Paper III: Laser-based powder bed fusion of interstitial nitrogen strengthened CoCrNi medium entropy alloy**
Sri Bala Aditya Malladi, Zhuoer Chen, Sheng Guo, Lars Nyborg
In manuscript

Contribution to the appended papers

Paper I: The author planned the work in collaboration with the co-authors. The corresponding author wrote the paper while main LB-PBF experimental work was performed by the author who also contributed towards finalizing the paper.

Paper II: The author planned and performed the experimental work. Analysis of results was performed in collaboration with the co-authors. The author wrote the paper with the help with of co-authors.

Paper III: The author planned and performed the experimental work. Analysis of results was performed in collaboration with the co-authors. The author wrote the paper with the help with of co-authors.

Table of Contents

CHAPTER 1	1
INTRODUCTION	1
1.1. Background	1
1.2. Objectives.....	3
CHAPTER 2	5
LASER BASED POWDER BED FUSION (LB-PBF).....	5
2.1 Principle	5
2.2 Microstructural evolution in LB-PBF	6
2.3 Influence of process conditions on the microstructural evolution.....	8
2.3.1 Influence of laser parameters	9
2.3.2 Influence of scan strategy	9
2.4 Columnar to equiaxed transition	10
2.4.1 Inoculation	11
2.4.2 Grain control by inoculation in LB-PBF.....	12
CHAPTER 3	15
SS441 FERRITIC STAINLESS STEEL	15
3.1 Microstructure and mechanical properties	16
CHAPTER 4	19
HIGH ENTROPY ALLOYS	19
4.1 Phase formation rules in HEAs	20
4.2 Medium entropy alloys	21
4.3 CoCrNi medium entropy alloy	22
4.3.1 Microstructure and mechanical properties	22

CHAPTER 5	25
METHODS	25
5.1 Laser based powder bed fusion (LB-PBF)	25
5.1.1 Printing of single tracks	25
5.2 Material Characterization	26
5.2.1 Metallography	26
5.2.2 Light optical microscopy.....	26
5.2.3 Scanning electron microscopy.....	27
5.2.4 X-ray diffraction	29
5.2.5 Hardness.....	30
5.2.6 Design of experiments.....	30
5.2.7 Thermodynamic calculations	31
5.2.8 Tensile testing.....	31
CHAPTER 6	33
SUMMARY OF RESULTS	33
6.1 In-situ inoculation in ferritic stainless steels	33
6.2 Influence of printing parameters on the microstructure of ferritic stainless steels.....	38
6.3 Effect of nitrogen doping in the CoCrNi MEA	40
CHAPTER 7	43
CONCLUSIONS.....	43
CHAPTER 8	45
FUTURE SCOPE.....	45

1.1. Background

The term additive manufacturing (AM) refers to a plethora of technologies that produce three-dimensional (3-D) parts by slicing them into multiple two-dimensional (2-D) layers from 3-D model data, as opposed to the subtractive manufacturing technologies. In 1984, Charles W Hull of 3-D systems created a first working 3-D printer and called it *Stereolithography Apparatus*^{1,2}. Though the technology was very expensive for that time, it paved way for the modern AM technologies such as powder bed fusion, material extrusion, direct energy deposition, binder jetting, etc. With the advancement of the AM technologies comes the advantages such as ability to manufacture complex geometries with relative ease, reduction in the amount of material waste, on-demand and customized manufacturing, high performance to weight ratio, reduced time to market, etc.²⁻⁶.

The AM processes can be classified into three main categories namely, i) liquid- based processes, ii) solid based processes, and iii) powder based processes⁷. According to ISO/ASTM standard 52911-1:2019⁸ the AM process can be categorized into seven main classes under the above-mentioned principles as shown in Figure 1. Among the AM processes, powder bed fusion technique uses high power energy source such as electron beam (electron beam powder bed fusion) and laser (laser-based powder bed fusion) to selectively melt and solidify powder to achieve full densification. Due to the intrinsic ability of powder bed fusion process to manufacture near net shape components, there is increasing demand in the applications mainly in the fields of automobile, aerospace, and biomedical fields.

In laser-based powder bed fusion (LB-PBF) process, quality of parts produced, and their characteristics depend on the physical phenomenon that take place as a result of

the interaction between the laser and the powder. Especially, the high cooling rates in LB-PBF result in some unique microstructures that are different from their cast counter parts. The local directional heat transfer during the solidification process also results in the columnar grain morphologies which may induce solidification cracking depending on solidification characteristics and anisotropy in the mechanical properties, whereby properties can tend to differ with respect to orientation in the produced parts. Owing to lack of materials designed for AM, there is an increasing need to develop alloys that are tailor made for the additive manufacturing.

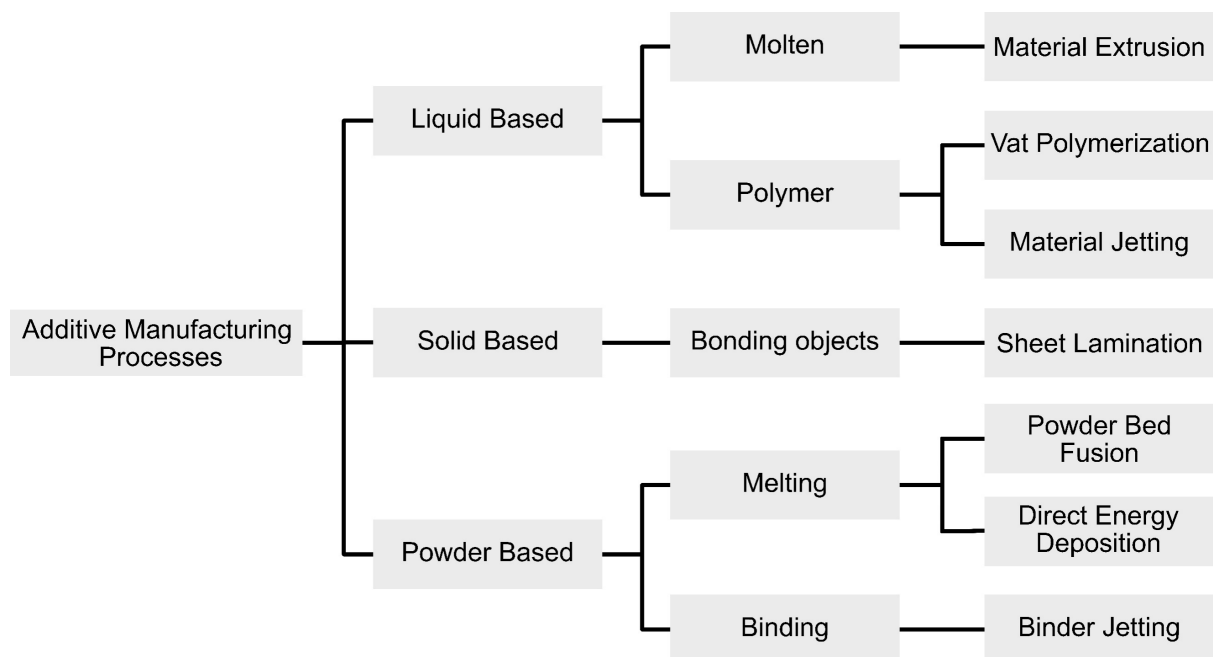


Figure 1 Overview of various additive manufacturing processes^{8,9}.

The alloy development strategies should mainly focus on i) reducing the solidification cracking/hot tearing by shortening the solidification range, ii) inducing the inoculation to promote equiaxed grain growth to suppress the formation of solidification cracks and to reduce the anisotropy and iii) improving the mechanical performance of the as-printed parts by taking advantage of the high cooling rate conditions and suppressing the formation of undesired phases and enhancing solid solution strengthening.

1.2.Objectives

The aim of this thesis study has been to understand the microstructural evolution of the high alloyed ferritic and austenitic materials produced through LB-PBF and based on this understanding, design and develop new alloys tailored for LB-PBF. In this respect, two different material systems were studied so far: SS441 (ferritic stainless steel) and CoCrNi without and with additional nitrogen as interstitial alloying element (interstitial medium entropy alloy). The objectives are divided into three main research questions as follows.

- 1. What is the influence of in-situ inoculation on the as-printed microstructure of ferritic stainless steel?*
- 2. What is the influence of printing parameters on microstructures of the inoculated ferritic stainless steel?*
- 3. What is the effect of nitrogen doping on the microstructure and mechanical properties of CoCrNi?*

LASER BASED POWDER BED FUSION (LB-PBF)

Powder bed fusion (PBF) processes form nearly 39% market share among all the AM processes available today. Laser based powder bed fusion (LB-PBF) is one of the powder bed-based AM technologies that allows the manufacturing of 3-D metallic components using high-power laser. The LB-PBF is known for having the widespread industrial adaptation among all the AM technologies¹⁰. The working principle, process steps and challenges associated with the LB-PBF process are discussed in the following sections.

2.1 Principle

A typical LB-PBF machine consists of a high-power fiber laser, galvano scanners, powder dispenser, build platform, excess powder collector and a re-coater. Schematic of the LB-PBF process is shown in Figure 2. The operation sequence of LB-PBF starts with a 3-D computer aided design (CAD) model of the part to be produced. This CAD model of the part is sliced into multiple two-dimensional (2-D) thin slices called layers. The information about the CAD design of the 3-D part and the sliced layers is transferred to the LB-PBF machine. Based on the information from the sliced 3-D model data, a thin layer of powder is applied on to the build plate. A high-speed laser then scans the selective regions on the build plate. The build platform is lowered to a predetermined height and a new layer of powder is recoated from the powder dispenser on the previous layer (already solidified layer) followed by melting and solidification. The process is repeated until the final part is produced. This entire process takes place inside a build chamber in an inert atmosphere (most commonly argon) to reduce the amount of oxygen intake during the printing process. Densification in LB-PBF is achieved through rapid melting and solidification of powder.

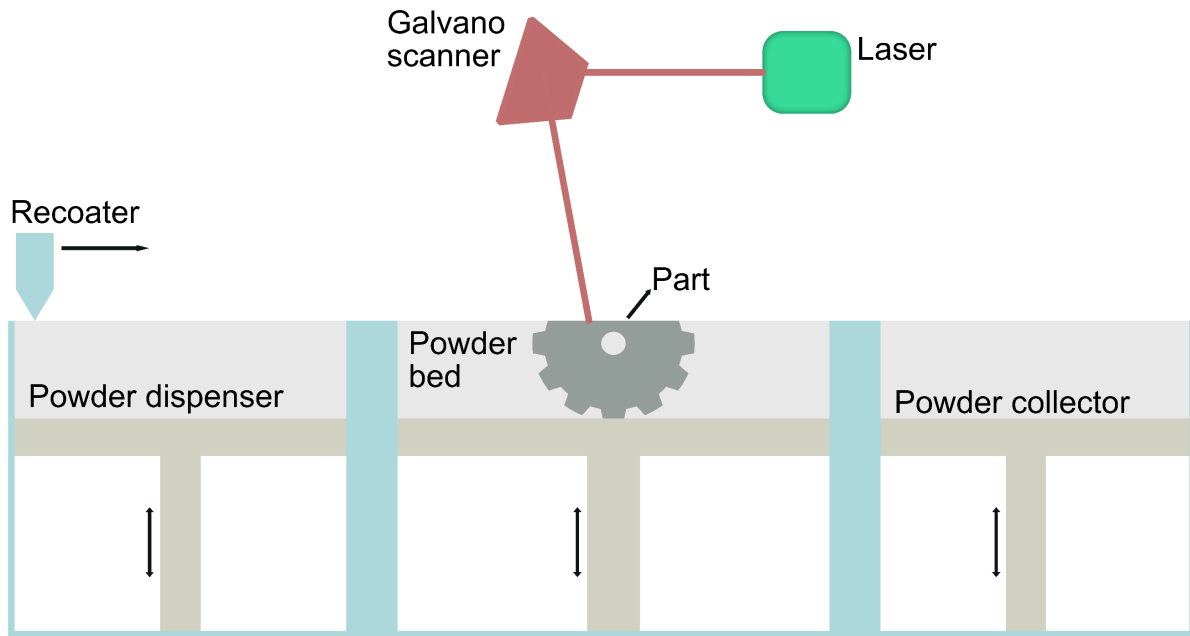


Figure 2 Schematic of the LB-PBF process.

2.2 Microstructural evolution in LB-PBF

Due to the rapid melting and solidification during the LB-PBF process, the metallic parts produced experience cyclic thermal stresses. The resulting thermal gradient, directional heat flow and high cooling rates have a significant influence on the dislocation density, grain size and solidification morphology. Due to the high cooling rates ($\sim 10^6$ K/s), elemental segregation is limited and at most confined to very fine solidification structure. This results in unique microstructures which have a direct influence on the resulting mechanical properties of the produced parts. The parts produced by means of LB-PBF usually tend to have higher strength than their cast counterparts¹¹. Like the welding process, the solidification in LB-PBF is governed by two main criteria namely, thermal gradient (G) and the growth rate (R). A schematic of the solidification mechanisms as a function of G and R are shown in Figure 3.

Once the laser interacts with the powder bed, it creates a melt pool which solidifies immediately as the laser moves away. The solidification starts at the pre-existing grains from the solidified layer below or from the build plate and hence this type of grain growth is termed as the epitaxial grain growth (Figure 17). Typically, this

epitaxial grain growth results in the formation of columnar grains spanning across a few layers due to the lack of nucleation events ahead of the solid/liquid interface. It should also be noted that the actual depth of the melt pool is always greater than the layer thickness. From the solidification theory, the grain morphology is mainly dominated by the G/R ratio. During the LB-PBF solidification, due to the focused energy input by the high energy laser, both G and R vary across the length of the melt pool. At the bottom of the melt pool, R is low, and G is high compared to the center of the melt pool. This results in the conditions that favour the formation of columnar grains at the edges of the melt pool in the orientation of the local thermal gradient. At the center of the melt pool on the other hand, G is at its lowest while R is highest resulting in the conditions favourable for formation of equiaxed grains. Hence, when the solidification starts at the bottom of the melt pools and the epitaxial growth of grains starts in multiple orientations. But as the grain growth is usually aligned with the maximum heat flow direction, in face centered cubic materials columnar grains should grow most commonly along the $\langle 100 \rangle$ crystallographic direction. As a result, the growth usually results in textured material with columnar grains.

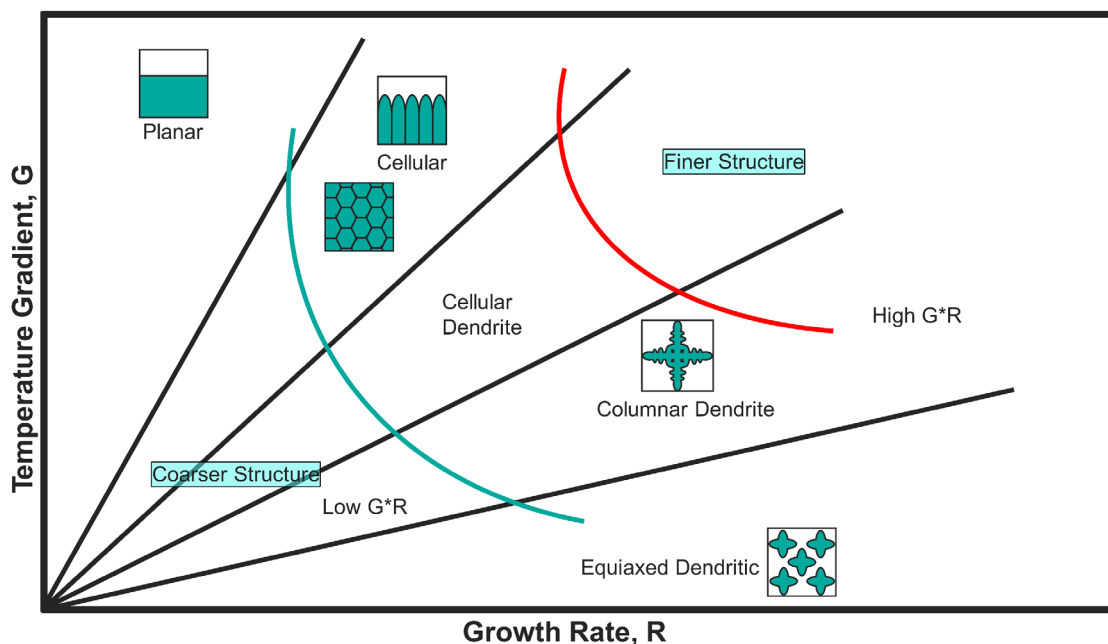


Figure 3 Schematic of the influence of thermal gradient (G) and growth rate (R) on the solidification mechanism¹².

2.3 Influence of process conditions on the microstructural evolution

The quality and properties of the parts produced by means of LB-PBF depend on various processing parameters. Among them, the most common ones are laser power, laser scanning speed, hatch distance, layer thickness and scan strategy. A schematic of the process parameters is shown in Figure 4.

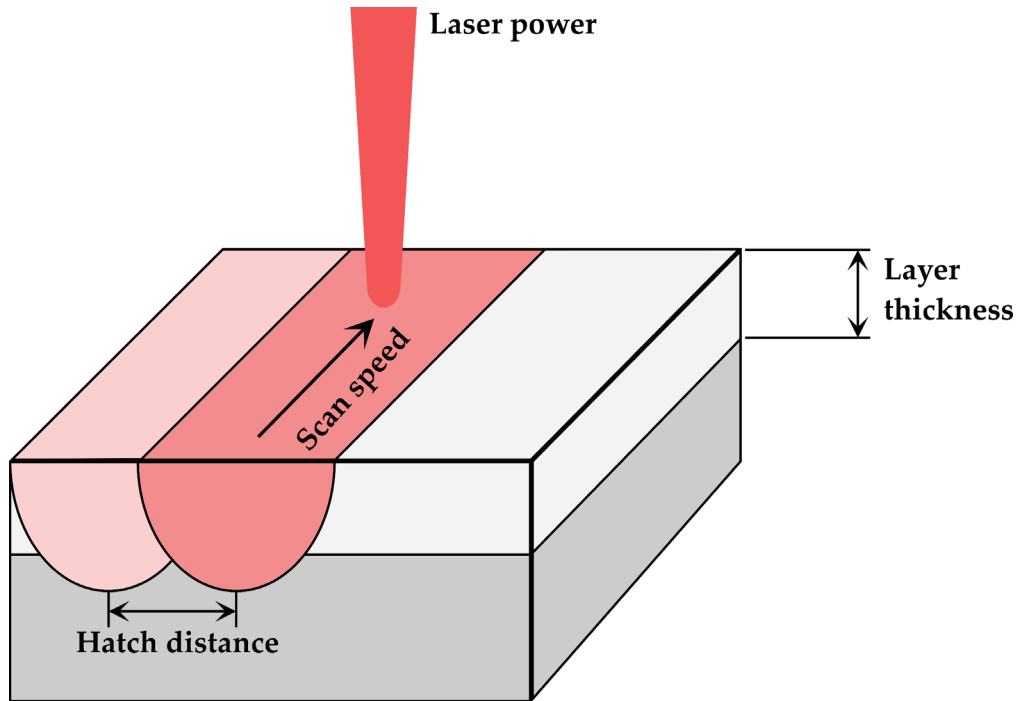


Figure 4 Schematic of the printing parameters in LB-PBF process.

In LB-PBF, the combination of the process parameters influences the shape and dimensions of the melt pool. This plays an important role in the resulting size, morphology, and orientation of grains. For example, for constant laser power, if the scan speed is varied, the size of the resulting melt pool varies¹³⁻¹⁷. At higher scan speeds, the resulting melt pool is relatively shallow while at lower scan speeds, the melt pool is deeper. Both G and R increase inside the melt pools as the scan speed increases. On the other hand, at a constant speed, G decreases as the power increases¹⁸. From the welding theory, it is reported that the scan speed plays an important role in the solidification. The scan speed determines the movement of the solidus/liquidus line which in turn determines the position of the growth interface^{14,16,18-21}.

2.3.1 Influence of laser parameters

Among the above-mentioned LB-PBF parameters, laser power and scan speed play a major role in the solidification dynamics and hence the grain growth. Increasing the laser power is reported to result in the increase in the grain size for titanium, steel, aluminum, and cobalt alloys^{14–16,22,23}. Materials printed at lower scan speeds are reported to have larger grains compared to the parts printed at higher scan speeds^{14,16,18,19,24–26}. Hatch distance has a huge influence on the melting in LB-PBF. Any change in the laser power or scan speed needs to be compensated with the hatch distance to achieve full densification. Low laser power or high scan speed need to be compensated with the shorter hatch distance and vice versa for the high laser power and low scan speeds. Though using the high scan speeds results in relatively finer grains inside the melt tracks, using the shorter hatch distance tends to increase the grain size due to the heat build-up by the adjacent tracks^{16,24,27}.

2.3.2 Influence of scan strategy

Other than the printing parameters, scan strategy also plays an important role in solidification dynamics and grain growth in the LB-PBF. One way to disrupt the columnar growth is by manipulating the scan strategy. Scan strategy is the spatial pattern and orientation in which the laser scans the layer. Figure 5 shows the schematics of the most common scan strategies in LB-PBF. Different scan strategies also affect the cooling rates and thermal gradients during printing.

Typically, a unidirectional scan strategy is known to result in a highly textured and elongated columnar grain growth in the building direction. This could be controlled by introducing the scan rotation between the successive layers. Even a 90° scan rotation is reported to weaken the texture and reduce the amount of the residual stresses and grain size^{22,23,26,28,29}. Some scan strategies are also reported to promote the side-branching because of the misalignment of G and the existing crystal there by reducing the epitaxial growth with change in the growth direction (from a typical $\langle 001 \rangle$ growth orientation in face centered cubic materials)³⁰.

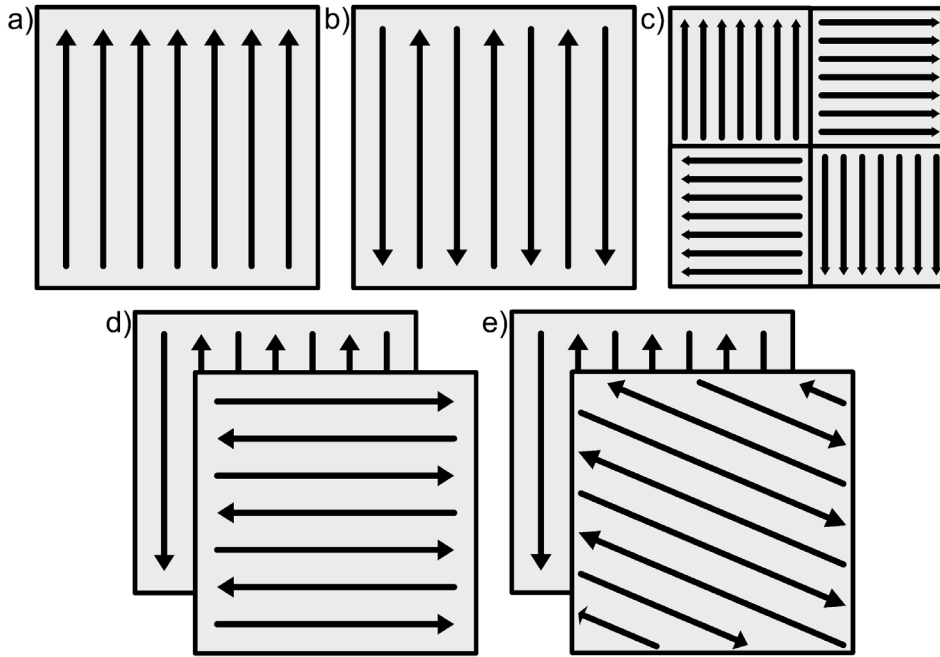


Figure 5 Schematic of most common scan strategies employed in LB-PBF a) unidirectional scan strategy b) bidirectional scan strategy c) chessboard scan strategy d) 90° rotation between the successive layers e) 67° rotation between the successive layers²².

While manipulation of the individual laser parameters and scan strategies could theoretically facilitate how they influence the G and R, their influence on the grain size control is very limited. This is because that, any variation in the laser power and scan speed needs to be compensated by hatch distance to achieve full densification. Though it is possible to refine the microstructure by manipulating the process parameters, the complexity of the process conditions inside the LB-PBF process makes it less practical.

2.4 Columnar to equiaxed transition

It is well known that metals and alloys under normal conditions, solidify with columnar grain structure both in casting and LB-PBF as discussed in the sections above. These columnar grains result in the anisotropy of the properties and hence not always desirable, whereas the presence of equiaxed grains is known to improve the isotropy of mechanical properties of the materials in general³¹⁻³³.

As discussed in Section 2.3, one way to achieve the columnar to equiaxed transition (CET) is by manipulating the process parameters and process conditions. But, even

with the manipulation of process parameters, the local heat flow is still directional, therefore the grain growth is still columnar. Another way to address the CET is by using inoculation to increase the number of heterogenous nucleation sites, hence, to promote the CET.

2.4.1 Inoculation

Solidification in alloys usually proceeds through undercooling which is the process of cooling the melt below the freezing point without the formation of the solid. This undercooling results in the formation of clusters and the cluster on attaining critical size grows into the nuclei. In case of homogenous nucleation, the degree of undercooling that is required to initiate the solidification could be few hundreds of degrees. This is practically impossible and in fact, nuclei form at significantly lower undercooling than the value required for homogenous nucleation due to the presence of active heterogeneities (solid particles in the melt) paving way for heterogenous nucleation.

One way to accelerate heterogenous nucleation is by the addition of nucleating particles called inoculants, which further reduce the degree of undercooling required for the formation of stable nuclei. Inoculation in metals and alloys is the addition of secondary particles to material in its molten state such that the inoculants act as heterogenous nucleating sites for the formation of equiaxed grains, while growth of columnar grains becomes suppressed^{31,34-36}. Inoculation is one of the most popular methods to achieve grain refinement due to its simplicity and the approach is widely used^{31,37,38}. For any particle to act as an inoculant, it should be able to properly wet the nucleating alloy. The contact between the inoculant and the matrix is usually treated by a spherical cap model and the equilibrium between the interfacial energies can be expressed as

$$\gamma_{lp} = \gamma_{sp} + \gamma_{ls} \cos\theta \quad (1)$$

Where γ_{lp} , γ_{sp} and γ_{ls} are the liquid/particle, solid/particle, and liquid/solid interfacial energies respectively and θ is the contact angle as shown in Figure 6.

For an inoculant to be effective, it should satisfy the following requirements:

- i) it should have higher melting point than the alloy being solidified,
- ii) it should be able to initiate freezing at very small undercooling,
- iii) number density of the particles in the melt should be high,
- iv) the nucleating particles should be larger than a critical size depending on the undercooling of the melt^{31,34}.

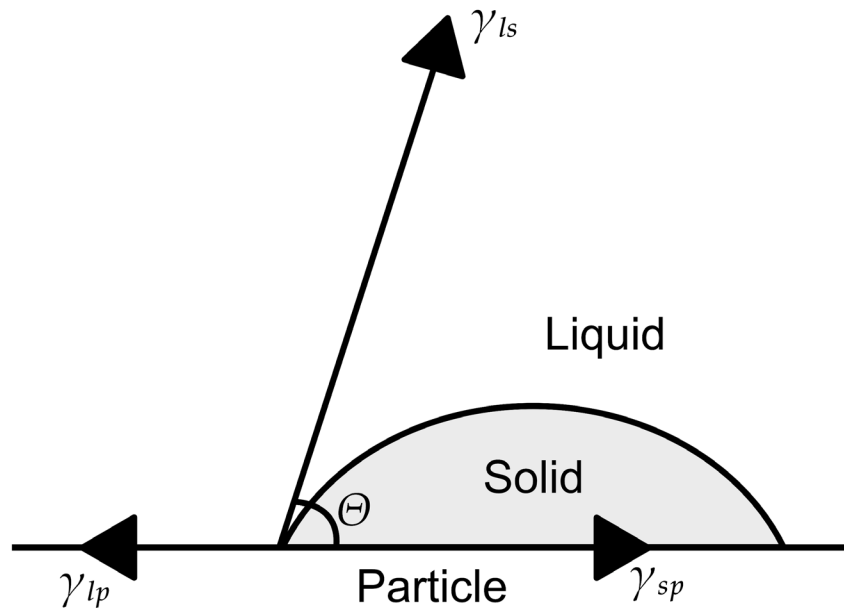


Figure 6 Spherical cap model depicting the equilibrium of interfacial energies between the solid, liquid, and the nucleating particle^{31,39}.

2.4.2 Grain control by inoculation in LB-PBF

As mentioned in the previous sections, because of the rapid melting and solidification mechanisms which result in a complex thermal gradients and solidification velocities, epitaxially grown columnar grains are common in LB-PBF. Addition of nucleating particles either in-situ (by alloy design) or by ex-situ additions to achieve the grain refinement has been studied for alloys such as Ti-6Al-4V (titanium alloy), aluminum alloys, iron based alloys and HEAs^{37,38,40}. Addition of elements such as boron, carbon, tungsten, and compounds such as TiN, La₂O₃ in particulate form to the Ti-alloys has proven to be better grain refiners owing to their ability to enhance the constitutive supercooling⁴¹. Their addition is reported to result in the refinement of prior- β grain size, refining the α -lath size and refinement of α -grains⁴⁰⁻⁴⁴. Potential applications and use cases for the aluminum alloys produced by LB-PBF for the aerospace applications

are high, owing to the advantages of the manufacturing route. However, apart from the anisotropy induced by the columnar grains, printing of some of the age-hardenable aluminum alloys such as 6000 and 7000 series is very challenging due to the hot cracking induced by the rapid melting and solidification conditions. Equiaxed grain structure resulting from the heterogenous nucleation with the help of inoculation in these aluminum alloys not only addresses the anisotropy but also addresses the hot cracking due to better distribution of the thermal strain in the fine grain structures. The grain size refinement in the 6000 and 7000 series aluminum alloys was reported to be achieved by the ex-situ addition of the hydrogen-stabilized zirconium nanoparticles. During solidification, the added nanoparticles react and form Al_3Zr which acted as inoculants³⁷. Similarly, addition of Ti-B is reported to induce a similar effect on the 2000 series aluminum alloys^{45,46}. This was reported to be achieved in-situ by alloy design to incorporate titanium which during solidification reacts with aluminum to form Al_3Ti , a well-known inoculant for aluminum alloys^{31,47}.

Among the grain refinement studies for the HEAs produced via LB-PBF, Cantor alloys are the only systems that were studied⁴⁸. Addition of the TiN nanoparticles ex-situ was shown to induce the grain size refinement resulting in change of strong $\langle 001 \rangle$ texture to random texture. The addition of TiN to this alloy system was reported to improve the yield strength of the alloy but decreases the ductility. However, the mechanism of grain refinement by the addition of TiN to Cantor alloy system is still unclear and needs further verification.

Though austenitic stainless steels (mostly 316L) are one of the widely studied alloys for LB-PBF, the grain refinement was mainly achieved by manipulating the printing parameters. The addition of particles such as MgO and NbO is known to influence the undercooling in casting conditions but not much work has been reported for LB-PBF conditions. Ferritic stainless steels, on the other hand, are gaining interest in the LB-PBF community due to their excellent printability and ability to solidify with fine equiaxed grains⁴⁹⁻⁵¹. The TiN is a well-known inoculant for the ferritic steels owing to

its low lattice misfit with the ferrite matrix and ability to increase the constitutional supercooling required for the heterogenous nucleation⁵². Ferritic stainless steel grade SS441, which is dual stabilized with niobium and titanium, is reported to form TiN in-situ during solidification in the presence of nitrogen⁵¹. Similarly, titanium alloyed ferritic steel grades are also reported to achieve excellent printability with a fine equiaxed grain structure^{49,50,53}.

SS441 FERRITIC STAINLESS STEEL

The most researched and used alloys for laser-based powder bed additive techniques include austenitic stainless steels, titanium alloys, aluminum alloys, cobalt-chrome, nickel-based super alloys, and copper-based alloys^{2,18,54-57}. Ferritic stainless steels have received little to no attraction in the field of additive manufacturing (AM). The SS441 stainless steel is one of the grades of the ferritic stainless steels which is mainly used in the automobile industry specifically for catalytic convertors. Materials for catalytic convertor applications require excellent thermal fatigue resistance and high temperature strength as the operating temperatures are as high as 900 °C. One of the biggest challenges for the utilization of ferritic stainless steels at these temperatures is, however, sensitization resulting in the depletion of chromium in the form of carbides. SS441 on the other hand is a titanium and niobium dual-stabilized steel, whose carbides are more stable than chromium carbides there by depleting the available carbon for sensitization⁵⁸. However, the presence of niobium poses a challenge by forming Laves phases which lead to embrittlement and loss of high temperature strength^{59,60}. The presence of Laves phase in SS441 is not always detrimental as in case of solid oxide fuel cells (SOFC), where SS441 is used as an interconnector. At the operating conditions of the SOFC's, niobium- and titanium- rich Laves phase interacts with silicon and prevent the formation of insulating silica layer⁶¹.

Table 1 Chemical compositions in weight percent of the alloy powders used in this study.

Material	Cr	Si	Mn	Nb	Ti	Ni	N	C	O	P	S	Fe
SS441	19.5	0.91	0.83	0.82	0.29	0.12	0.1	0.035	0.032	0.015	0.007	Balance
Ti-free	18	0.7	0.8	-	0.01	0.1	0.1	0.01	0.1	0.01	0.01	Balance
High-Ti	19.5	0.9	0.9	-	0.8	0.2	0.12	0.02	-	0.01	0.01	Balance

3.1 Microstructure and mechanical properties

The traditional manufacturing method for SS441 is by casting and hot rolling with a relatively equiaxed microstructure of grain size around 50 μm with a distribution of TiN particles inside the grains and Nb (C, N) particles at the grain boundaries^{51,59,60,62}. However, due to the high thermal gradients and solidification velocities in the LB-PBF process, SS441 is known to undergo cellular solidification with niobium segregating into the cell walls, while titanium-rich oxides occur inside the grains with an average grain size of about 1.6 μm ⁵¹. On annealing, the niobium-rich cell walls assist in the formation of Laves phase. The SS441 manufactured by means of LB-PBF is shown to exhibit high yield strength ($\sim 680 - 740$ MPa), attributed to the relatively smaller grain size and cellular solidification structure compared to its wrought counter parts (~ 314 MPa)⁵¹.

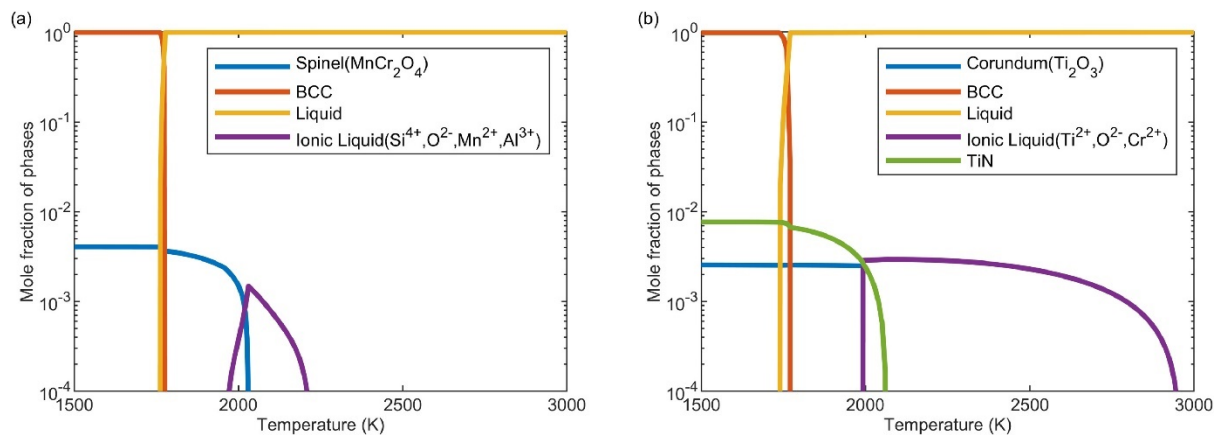


Figure 7 Phase fractions at equilibrium as a function of temperature calculated for the (a) Ti-free and (b) Ti-high as-built compositions listed in Table 1⁵³.

Three different variants of pre-alloyed gas-atomized powder based on SS441, supplied by Kanthal AB, with particle size distribution ranging from 10 to 45 μm , were used in this study. The chemical composition of the stainless-steel powder variants under the present study is mentioned in Table 1. This part of the study has been based on close co-operation between Chalmers University of Technology, Gothenburg and Royal Institute of Technology, Stockholm, whereby computational thermodynamic models based on CALPHAD were employed by Associate Professor Greta Lindwall and Dr. Durga Ananthanarayanan at Royal Institute of Technology, to design the alloy in

order to i) to maximize the amount of TiN available during the solidification, and ii) to minimize the possibility of formation of detrimental phases such as Laves phase, which depletes the titanium available to form TiN as shown in Figure 7.

Traditional alloying as we know today has been around for millennia with the idea of using a *base metal* with some attractive properties and selectively adding other elements in *minor quantities* to that base metal in order to improve properties. This concept of alloying barely scratches the edges of the phase diagram. With the ever-growing advancements in technologies, there is a need for improving the properties of the existing materials that are heavily dependent on the existing base elements. For example, energy and aerospace industries need improved high temperature properties, while lighter and cheaper alloys are requested in general for the transportation sector. In 2004, two research groups namely, Cantor et al.⁶³ and Yeh et al.⁶⁴ simultaneously tried to address this with a new concept of alloys called high entropy alloys (HEAs). This new concept of alloying tried to explore the center of the multi-element phase diagram and where there is no obvious base element.

The original definition of the HEAs is based on the entropy effect. Yeh et al.⁶⁴ hypothesized that for an ideal solid solution (enthalpy of mixing, ΔH_{mix} is zero), the free energy of formation of the alloy depends mainly on the entropic part as shown in the equation below:

$$\Delta G_{\text{mix}} = -T\Delta S_{\text{mix}} \quad (2)$$

where, ΔG_{mix} is the Gibbs free energy of mixing, ΔS_{mix} is the entropy of mixing and T is the absolute temperature. Boltzmann's equation for ideal entropy of mixing is given by:

$$\Delta S_{\text{mix}} = -R\sum x_i \ln x_i \quad (3)$$

where, R is the gas constant and x_i is the mole fraction of the i^{th} element. If the alloy is an equiatomic alloy with n elements, the above equation changes to

$$\Delta S_{mix} = -R \ln n \quad (4)$$

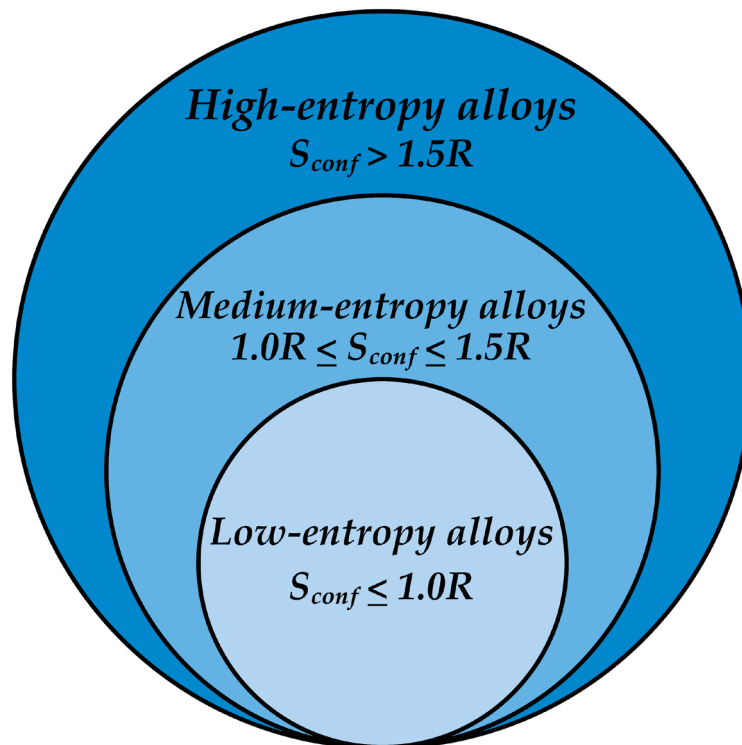


Figure 8 Classification of alloys based on their value of entropy of mixing⁶⁵.

Using the above equation for the configurational entropy of mixing, the values for entropy of mixing for equiatomic alloys with 4, 5 and 6 elements are $1.39R$, $1.61R$ and $1.79R$, respectively. Based on this, the HEAs were originally defined as the alloys with at least 5 elements with the elemental concentrations between 5 and 35 atom percent. At values greater than $1.6R$, the contribution of mixing entropy becomes more significant to the total free energy of the system that, it could overcome the mixing enthalpies of forming intermetallics and phase separation. Depending on the magnitude of the mixing entropy, the alloys are classified as low-entropy alloys, medium entropy alloys (MEAs) and HEAs, as shown in Figure 8⁶⁶⁻⁶⁸.

4.1 Phase formation rules in HEAs

While the entropic stabilization can explain to some extent why some of the HEAs contain single phase solid solutions, it does not fully explain the formation of intermetallics, complex compounds and even the amorphous phase⁶⁹⁻⁷³.

Zhang et al. and Guo et al.^{74,75} tried to explain the phase formation rules by considering the factors such as *enthalpy of mixing* (ΔH_{mix}), *entropy of mixing* (ΔS_{mix}), *atomic size difference* (δ), *electronegativity difference* ($\Delta\chi$) and *valence electronic configurations* (VEC). They concluded that high configurational entropy of mixing is not the only factor that controls the formation and stabilization of the phases in HEAs, and solid solutions can form when

$$-22 \leq \Delta H_{mix} \leq 7 \text{ kJ/mol},$$

$$0 \leq \delta \leq 8.5 \text{ and}$$

$$11 \leq \Delta S_{mix} \leq 19.5 \text{ J/(K}\cdot\text{mol)}$$

On the other hand, VEC plays an important role in determining whether FCC or BCC solid solutions are formed. They concluded that $VEC \geq 8$ favours FCC type solid solution and $VEC \leq 6.87$ favours the formation of BCC solid solution and a mixture of BCC and FCC solid solution forms with $6.87 \leq VEC \leq 8.0$ ⁷⁴⁻⁷⁸. Apart from the above-mentioned parameters that influence the phase stability and formation of various solid solutions in HEAs, a few more empirical parameters were suggested by researchers, which provide additional insights into phase formation⁷⁸⁻⁸⁰. However, a clear understanding of phase stability is still lacking, especially for the solid solution types other than FCC and BCC⁷⁷.

4.2 Medium entropy alloys

Classification of the HEAs based on the configurational entropy of mixing has been mentioned in the previous section. Based on that classification, if the configurational entropy of mixing is between 1R and 1.5R, then those alloys are called medium entropy alloys (MEAs). These alloys are either equiatomic with the number of principal elements less than 5 (example ternary alloys or quaternary alloys) or are non-equiatomic. Some of the examples of MEAs are CoCrNi, CoNiV, CoCrFeNi, Ni₄₆Cr₂₃Co₂₃Al₄Ti₄, etc. Even though these alloys are MEAs, they have shown

exceptional phase stability and even superior properties compared to their HEA counter parts^{69,81-85}.

4.3 CoCrNi medium entropy alloy

Equiatomic single-phase face centered cubic CoCrNi is the most widely studied MEA owing to its high strength and ductility, excellent corrosion and oxidation resistance, enhanced hydrogen embrittlement resistance and excellent cryogenic properties^{82,85-89}. It is also known to provide high strain hardening due to its ability to undergo deformation twinning upon plastic deformation as a result of its low stacking fault energy (SFE)⁸¹.

4.3.1 Microstructure and mechanical properties

Typical microstructure of cast CoCrNi alloy was reported to have grain size of about 4 μm post recrystallization⁸⁵. Recrystallization in CoCrNi alloy was also known to form nano twins due to its intrinsically low SFE, resulting in high strain hardening. The tensile strength and ductility in CoCrNi could exceed 1.4GPa and 90%, respectively, at 77K, making this alloy one of the most damage tolerant alloys⁸⁵. The addition of interstitial elements is also known to improve the mechanical properties by interstitial solid solution strengthening and lowering the SFE, therefore further enhancing the twinning-induced plasticity.

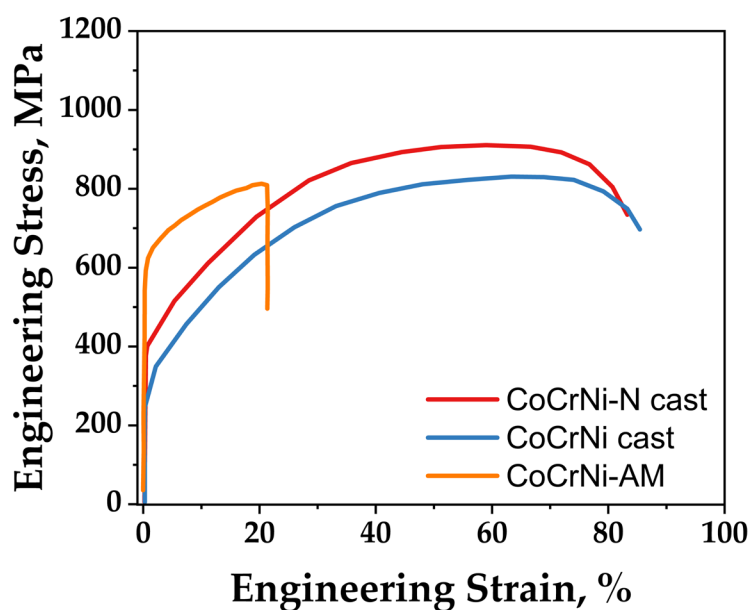


Figure 9 Tensile properties of cast and AM CoCrNi and CoCrNi-N MEAs (redrawn from^{90,91}).

Addition of nitrogen or carbon as an interstitial to CoCrNi alloy was observed to enhance its yield strength, high temperature properties and corrosion resistance^{90,92-94}. Nitrogen addition was also reported to slow down the grain growth of the alloy post-annealing treatment due to the precipitation of Cr₂N^{90,93}. Microstructure of additively manufactured CoCrNi alloy was reported to undergo cellular segregation due to the steep thermal gradients and high solidification velocities, with an average grain size of about 25 μm in the as-printed state⁹¹.

This chapter provides a brief overview of the experimental techniques used in this thesis study and their respective background.

5.1 Laser based powder bed fusion (LB-PBF)

All the samples manufactured in this study were printed using an EOS M100 (EOS GmbH) machine equipped with a 200W Yb-fiber laser with a spot diameter of 40 μm . This machine features a circular build plate of 100 mm diameter with a maximum build height of 95 mm. The build chamber was flooded with argon gas prior to the printing to maintain the oxygen levels inside the chamber below 1000 ppm. Cubic samples of 10 x 10 x 10 mm³ were produced using custom set of parameters optimized in-house at Department of Industrial and Materials Science, Chalmers University of Technology. The samples were printed using a stripe scan strategy (Figure 10) with a stripe width of 5 mm and an overlap of 0.1 mm between the stripes. A 67° scan rotation was used between the subsequent layers.

5.1.1 Printing of single tracks

To understand the effect of inoculants on the grain refinement of the printed bulk parts, single scan tracks were also printed on the bulk samples manufactured from the respective materials.

Single scan tracks of 8 mm length and 10 layers high were in this way printed at 110 W laser power and 20 μm layer thickness and at scan speeds of 600 mm/s, 800 mm/s and 1000 mm/s on the surface of the bulk sample of dimensions 10 x 10 x 3 mm³ as shown in Figure 10. For each material, the single scan track of 1 layer height or 10 layers height were printed using the above mentioned parameters.

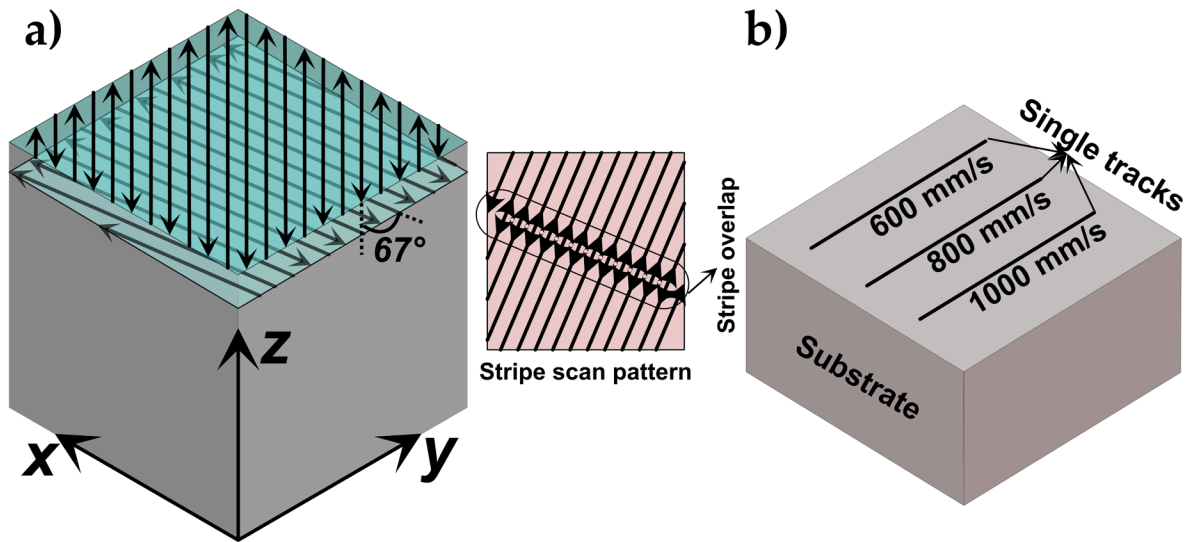


Figure 10 Schematic a) showing scan rotation, stripe scan strategy and b) single tracks printed on a substrate.

5.2 Material Characterization

5.2.1 Metallography

Metallographic preparation of the powder samples was carried out by mixing small quantities of alloy powder with PolyFast by Struers, a conductive mounting resin followed by hot mounting with Citopress-20 (Struers). Bulk samples, removed from the build plate using the wire EDM, were mounted in the same way as the powder sample. The mounted samples were first ground using a 320-grit silicon carbide grinding paper to get a flat surface. This was followed by sequential polishing using 9 μm , 3 μm and 1 μm suspended diamond solutions. These steps were followed by final polishing using colloidal suspension of silica particles (~ 50 nm) on an oxide polishing cloth to get a mirror like sample surface. Etching of the MEAs was done using diluted aqua regia (1:3 volume mixture of nitric acid and hydrochloric acid) to reveal the cellular solidification structure.

5.2.2 Light optical microscopy

Light optical microscope (LOM) is one of the most basic, yet most useful tools in the metallurgical analysis. LOM uses visible light as the light source which when reflected from the sample surface, passes through a set of lenses to magnify, and form an image.

Although modern microscopes have a complex design to improve the resolution and contrast of the image down to a few micrometers, the resolution is still limited due to the limited wavelength of the visible light.

The polished samples were observed under Zeiss Axioscope 7 microscope equipped with Zeiss Axiocam 105 colour camera. The imaging was performed at 100X magnification by acquiring stitched images of the samples. The acquired images were then processed using FIJI ImageJ freeware for porosity analysis using the contrast threshold method⁹⁵.

5.2.3 Scanning electron microscopy

The main difference between the LOM and scanning electron microscope (SEM) is the source of imaging, where SEM uses accelerated beam of electrons (usually between 1 keV and 30 keV). The electrons generated at cathode are focused into a spot on to the surface of the sample using a set of condenser lens. While both visible light and electrons are part of the electromagnetic spectrum, the wavelength of the visible light is between 400 nm and 700 nm, whereas the wavelength of the electrons varies from 0.001 nm to 0.01 nm. This results in a theoretical resolution of about 0.02 nm for an electron microscope. Another major difference between LOM and SEM is that the electrons are strongly scattered by gases than the visible light. Hence, it is required to maintain a vacuum level of at least 10^{-7} atmospheric pressure inside an electron microscope. While the lenses in the optical microscope have refractive index, which contribute to the limited resolution of the optical microscopes, the "lenses" in the electron microscopes are essentially magnetic fields and hence there is a negligible change of the refractive index as the electrons pass through each magnetic lens.

When accelerated high energy electrons interact with the material, they penetrate the sample to a depth of a few microns depending on the accelerating voltage and the density of the sample. The interaction between the electron beam and the sample produces elastic and inelastic collisions with the atoms of the material and results in scattering of electrons with a wide range of energies. Depending on the type of

interaction, different signals like secondary electrons (SE), backscattered electrons (BSE), diffracted backscattered electrons (EBSD), characteristic and continuum X-rays, and heat are generated. These signals are collected by one or more types of detectors. Images are generated from these collected signals and are then displayed on the screen⁹⁶. The representative electron-material interaction is shown in Figure 11.

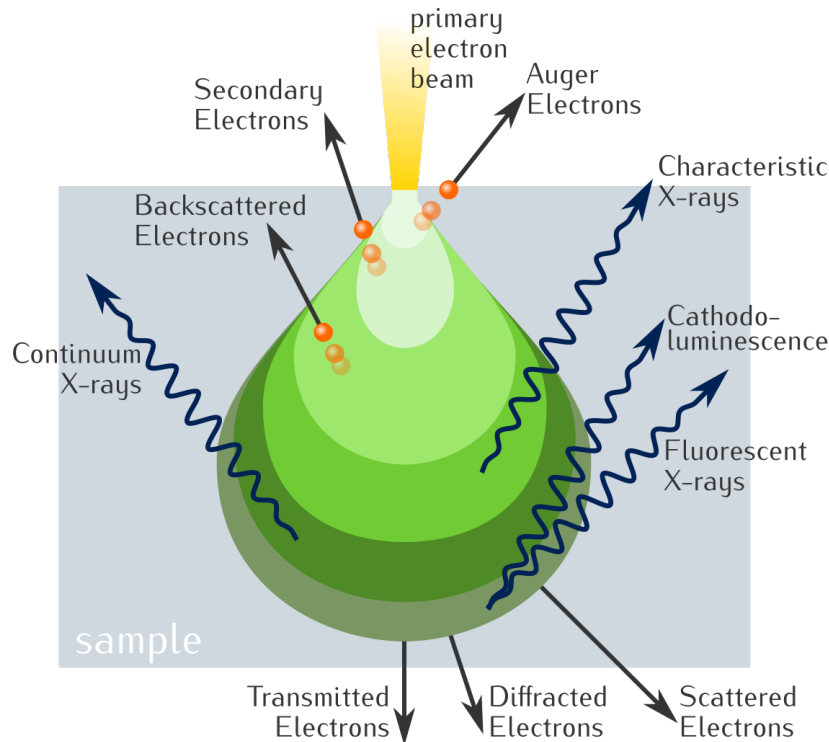


Figure 11 Origin and information of secondary electrons, backscattered electrons, Auger electrons, X-rays (X) in the diffusion cloud of electron range R for normal incidence of primary electrons⁹⁷.

Microstructural characterization of both the printed bulk samples and the powder was performed using LEO Gemini 1550 and LEO Gemini 450 field emission gun scanning electron microscopes (FEGSEM). Energy dispersive X-ray spectroscopy (EDS) was performed to analyze the elemental composition of various phases in the microstructure using X-Max EDS detector. Electron back scattered diffraction (EBSD) was performed to understand the crystallographic orientation of the printed samples with respect to various building directions using Nordlys II detector by Oxford Instruments. The analysis of the EBSD data was performed using MTEX, an opensource MATLAB toolbox⁹⁸.

5.2.4 X-ray diffraction

X-ray diffraction (XRD) is one of the most used techniques to determine the phase information, crystallinity, and texture of the materials as the wavelength of the X-rays (typically vary between 0.2 to 10 nm) are comparable to the interatomic spacing of the crystalline solids. When X-rays from a monochromatic source of wavelength, λ , are impinged on to a crystalline material, the interaction results in the constructive interference as shown in Figure 12 which can be described/determined by the Bragg's law as mentioned below:

$$n\lambda = 2 * d * \sin\theta \quad (5)$$

where d is the interplanar spacing, θ is the diffraction angle and n is the order of diffraction. This constructive interference results in the peaks which are then matched using powder diffraction files (PDF) database of the standard diffraction patterns. The peak positions in XRD patterns represent the miller indices hkl of the plane at which the constructive interference occurs⁹⁹. The lattice parameter for cubic materials could be obtained by using the equation given below

$$\frac{1}{d_{hkl}^2} = \frac{h^2+k^2+l^2}{a^2} \quad (6)$$

where a is the lattice parameter.

In this study, the phase characterization of the materials was performed using Bruker AXS D8 Advance diffractometer equipped with a Cr $K\alpha$ source ($\lambda = 2.28970 \text{ \AA}$) operated at 35 kV and 40 mA.

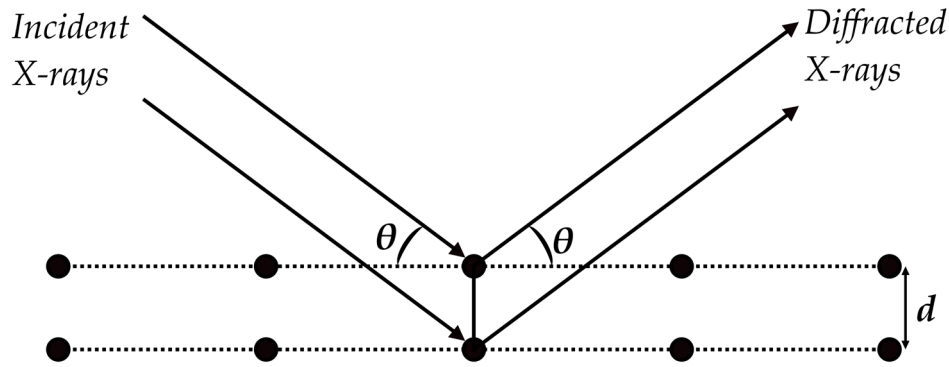


Figure 12 Schematic representation of the principle of X-ray diffraction⁹⁹.

5.2.5 Hardness

Hardness of a material, defined as the *resistance to plastic deformation* is one of the most crucial properties to assess the component quality for various applications. Vickers hardness is one of the indentation hardness techniques which uses a diamond indenter shaped in the form of an inverted pyramid with 136° angle between the opposite faces. Once the material is indented using a predetermined load (L), the length of the diagonals is measured, and the hardness is calculated using the following equation

$$HV = \frac{L}{A} = \frac{1.8544L}{d^2} \quad (7)$$

where d is the average length of the two diagonals of the indent.

Vickers hardness measurements for the materials used in the study were made using Struers Durascan-70 G5 at 1 kgf load for 15 s of dwell time on the polished materials. The hardness values were taken in both building and transverse directions of the printed samples to measure the anisotropy with respect to different directions.

5.2.6 Design of experiments

Design of experiments (DOE) methodology is a statistical approach to depict the influence of experimental parameters to predict the outcome. The DOE is a very powerful tool that saves time and resources especially for processes like LB-PBF. It is

used for understanding the influence of various process parameters such as laser power, hatch distance, scan speed and layer thickness on the resulting densification of the samples.

Since the materials used in this study do not have a standard set of parameters from the machine manufacturer, the DOE methodology was employed to understand the influence of above-mentioned process parameters on the resulting densification. The JMP software (from the SAS Institute, Cary, NC, USA) was used and a 2-factor D-optimal design was employed by varying hatch distance and scan speed and the laser power (110 W) and layer thickness (20 μm) were kept constant.

5.2.7 Thermodynamic calculations

Thermodynamic calculations were performed using ThermoCalc¹⁰⁰, a commercial CALPHAD (CALculation of PHAse Diagram) software, using TCHEA4 database for HEAs and TCFE10 database for ferritic steels. With the help of thermodynamic calculations, the potential phase fraction for the alloys used in this study were predicted and the alloy compositions were tweaked accordingly to reduce the probability of formation of detrimental phases. Scheil solidification simulations were performed to predict the solidification pathway for the alloys and obtain an understanding about the elemental segregation during solidification.

5.2.8 Tensile testing

Tensile samples of gauge length 12.5 mm, width 2.5 mm and thickness 1 mm were obtained through electric discharge machining from bulk samples of dimensions 55 mm x 10 mm x 10 mm. The tensile tests were performed on Instron 5500R tester at a constant strain rate of 10^{-3} s^{-1} and to a maximum of 40 % engineering strain.

6.1 In-situ inoculation in ferritic stainless steels

Three different variants of ferritic stainless steels based on SS441 were studied in order to i) maximize the amount of titanium and nitrogen available for the formation of TiN particles prior to the solidification of ferrite matrix, and ii) minimize the formation of intermetallic Laves phase ($\text{Fe}_2(\text{Ti,Nb})$) and σ -phase which could potentially be detrimental to the mechanical performance of the materials (Table 1 and Figure 7). All the three materials were printed with the same set of printing parameters and the orientation maps obtained from EBSD analysis of the as-printed materials in x-y and x-z orientations are shown in Figure 13.

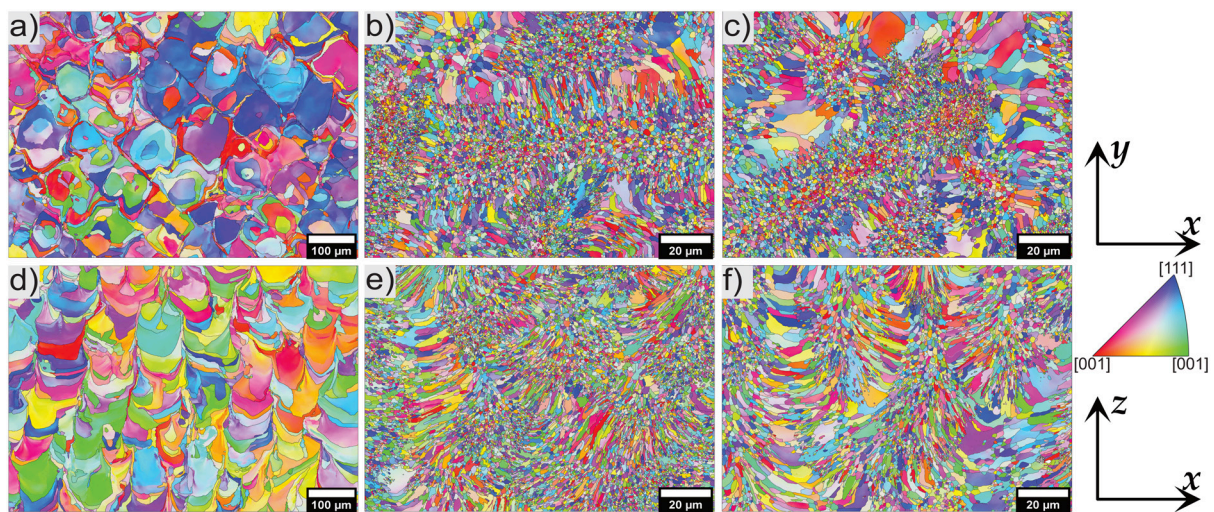


Figure 13 EBSD orientation maps of Ti-free (a, d), SS441 (b, e), and Ti-high (c, f) material in x-y and x-z orientations.

Comparing all the three materials with respect to different building directions, it is clear that SS441 and the Ti-high material showed completely different microstructure compared to Ti-free material. The Ti-free material revealed epitaxially grown large columnar grains in the x-z orientation and similar large grains spanning across a few scan tracks as seen in the x-y orientation, which is typical for LB-PBF process conditions (Figure 13a, d). For SS441 (Figure 13b, e) and the Ti-high material (Figure 13c, f), the microstructure showed a mixture of fine equiaxed grains and some long

columnar grains. The average grain size measured from EBSD data for the Ti-free material is $\sim 14 \mu\text{m}$, whereas for both SS441 and the Ti-high material the average grain size is $\sim 1 \mu\text{m}$. Figure 14 shows the pole figures of the Ti-free material (Figure 14a), SS441 (Figure 14b), and the Ti-high material (Figure 14c). Influence of titanium content is also clear in terms of the texture with the Ti-free material showing $\langle 001 \rangle$ texture in the building direction, while the SS441 and the Ti-high material show more random $\langle 111 \rangle$ texture. This difference in texture indicates the difference in the solidification behaviour between Ti-free and Ti-containing materials.

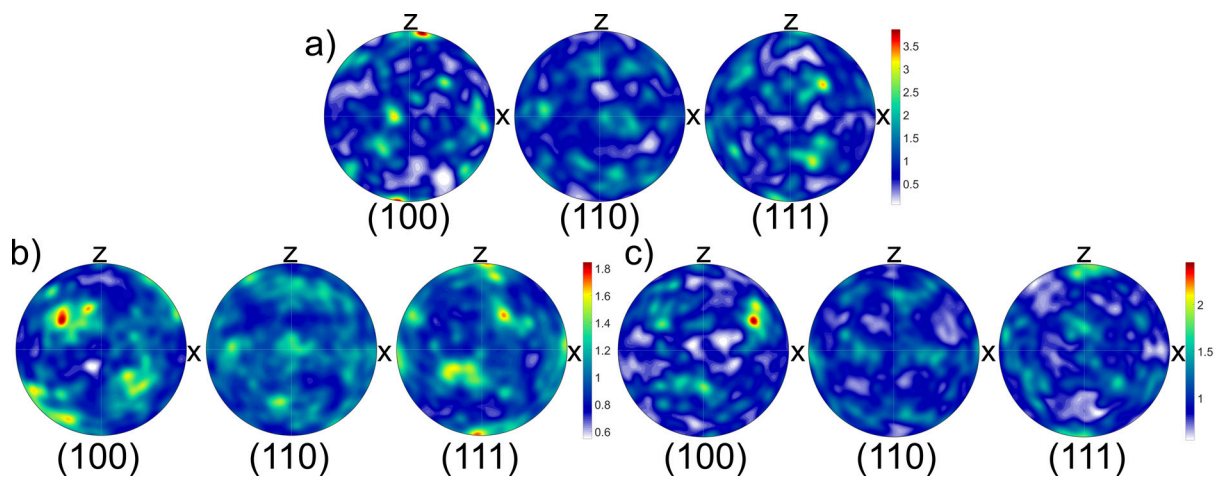


Figure 14 Pole figures for a) the Ti-free material, b) SS441 and c) the Ti-high material in x-z orientation.

In order for an inoculant to be effective, it should have i) low lattice mismatch with the matrix, and ii) should be able to wet the nucleating solid effectively³¹. Apart from the above-mentioned points, number density and size of the inoculant particles are also of utmost importance^{34,36}. Titanium nitride is known to be one of the most effective inoculants for the ferritic steels due to its low lattice mismatch and better wetting of the ferrite in the cast alloys^{52,101,102}.

Microstructural analysis revealed the distribution of various particles in all the three materials under investigation (Figure 15a, b, c). The EDS analysis of particles in the Ti-free material (Figure 15d) revealed the presence of spherical Al-Si-containing oxides. The SS441 and the Ti-high material (Figure 15e and f) showed the distribution of pure

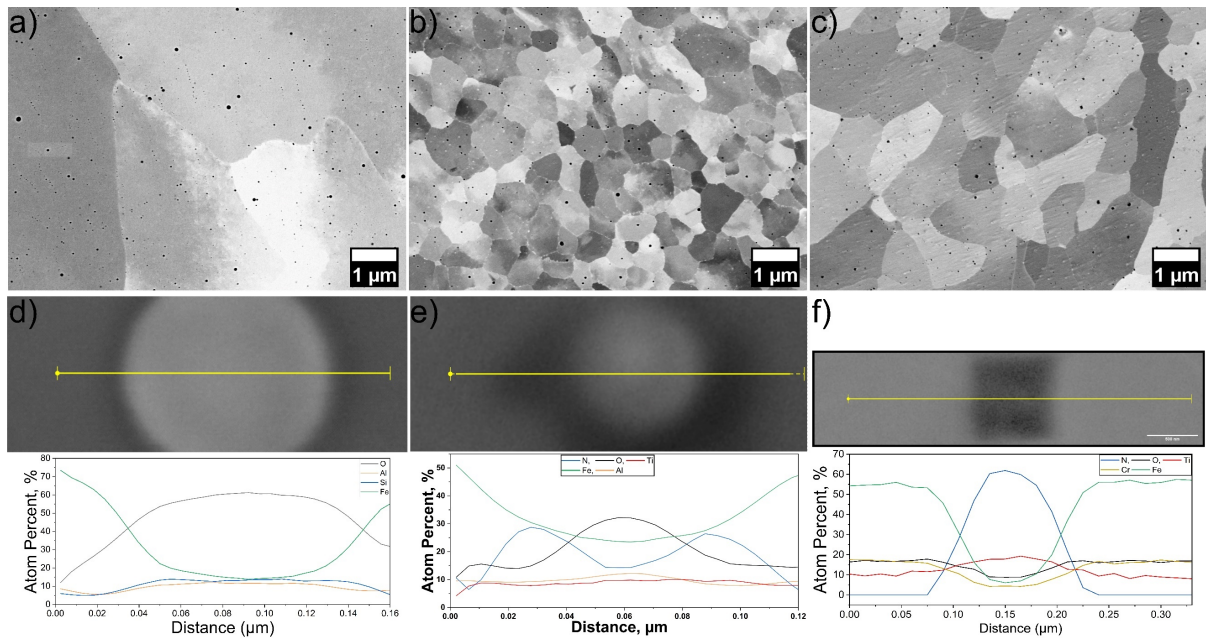


Figure 15 SEM backscattered electron images of a) the Ti-free material, b) SS441, and c) the Ti-high material showing the distribution of particles inside the matrix, and EDS analysis of the particles in d) the Ti free material showing Al-Si oxides, e) core-shell type oxy-nitride particles and f) pure nitride particles in SS441 and the Ti-high material.

titanium nitrides and core-shell structured oxy-nitrides with aluminum-rich oxide core and titanium nitride shell. Though a clear influence of titanium addition on the solidification behaviour and grain refinement of these alloys was seen, a mixture of columnar and equiaxed grains was observed in both the SS441 and the Ti-high material.

In order to get a better understanding of the efficiency of TiN as an inoculant for the LB-PBF processing conditions, it is necessary to develop an understanding of the distribution of TiN particles inside the ferrite matrix. Automated feature analysis of the particles combined with EDS was performed for the equiaxed and columnar regions of the SS441 and the Ti-free material and the size distributions are shown in Figure 16.

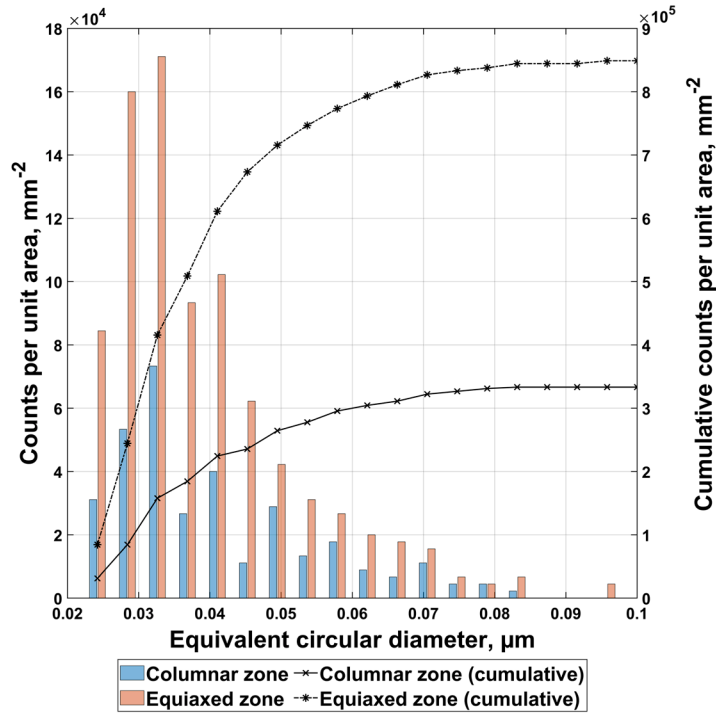


Figure 16 Automated feature analysis of the particles showing the size distribution of particles in columnar and equiaxed regions.

It is clear from Figure 16 that the number of particles in the equiaxed region are much higher than that in the columnar region. However, the average size of particles in both equiaxed and columnar region are very similar, ~ 39 nm, while as said the number density of particles in the columnar region is $\sim 0.3 / \mu\text{m}^2$, whereas $\sim 0.9 / \mu\text{m}^2$ in the equiaxed region. If one considers the solidification at the melt pool scale, at the bottom of the melt pool, G is high, and V is low, resulting in conditions favourable for the columnar growth. In order to promote CET in this columnar region, the required number density and size of the inoculating particles must be higher to achieve undercooling required for the equiaxed growth. At the center of the melt pool, on the other hand, G is low, and V is high. These conditions are more favourable for the formation of equiaxed grains. Also, at the center of the melt pool, the alloy stays molten for relatively longer periods compared to at the edges of the melt pool, thereby providing sufficient time for the nucleation and growth of inoculant particles and resulting in the equiaxed grains. A schematic of different thermal conditions within one melt pool and its resulting influence on the grain morphology are shown in Figure 17.

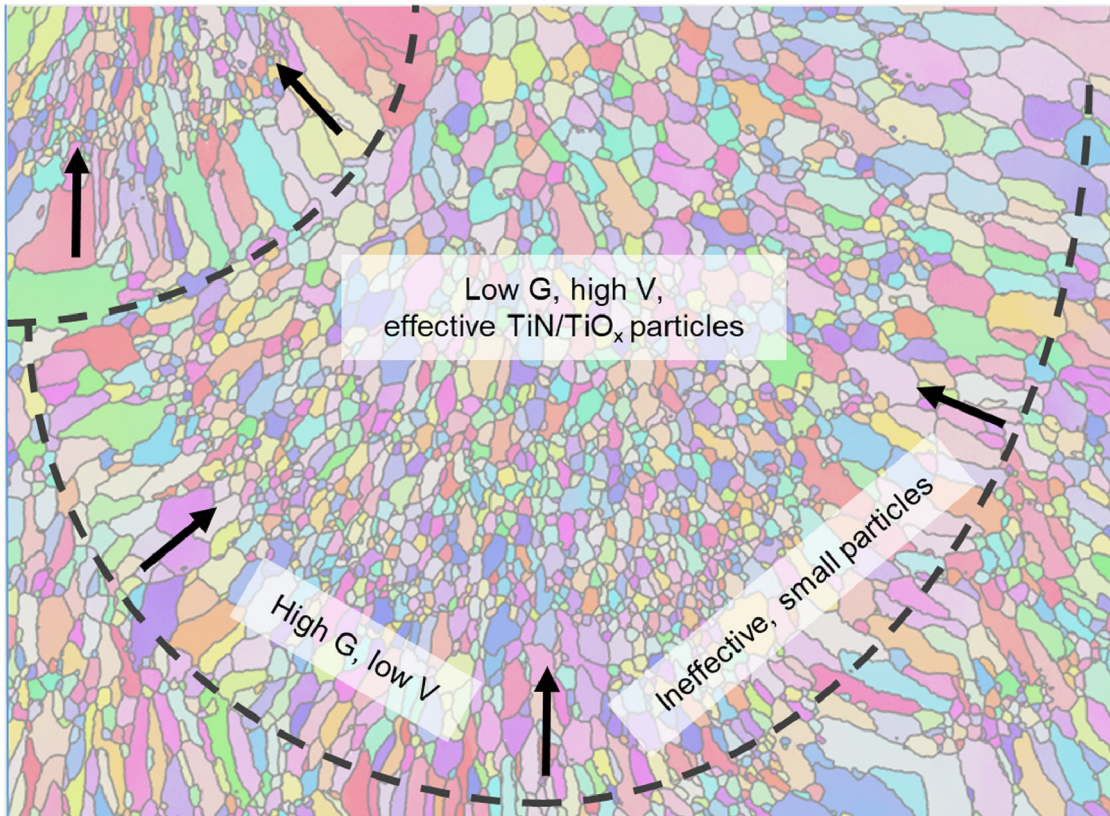


Figure 17 Schematic showing the difference in the G and V at different regions of the meltpools that influence the grain morphology⁵³.

6.2 Influence of printing parameters on the microstructure of ferritic stainless steels

As mentioned in the previous section, the concept of in-situ inoculation has been very effective in terms of influencing the solidification conditions, resulting in a 20-fold reduction in grain size for the inoculated materials. However, the microstructure still consists of a mixture of columnar grains and equiaxed grains. It is well reported that in LB-PBF, manipulation of process parameters could result in the formation of equiaxed grain structures¹⁴⁻¹⁶. Specifically, either an increase in the laser power or an increase in the scan speed was reported to lower G and increase V during solidification within the melt pool, resulting in finer grain size. In order to understand the influence of printing parameters on the resulting grain morphology, single tracks were printed at scan speeds of 600, 800 and 1000 mm/s at a constant laser power of 110 W and layer thickness of 20 μm . The resulting grain size distribution of single tracks in comparison with the bulk materials are shown in Figure 18.

A similar trend was observed from the grain size distribution plots for single tracks from all the three materials. Tracks printed at high scan speeds showed finer grain sizes relative to the tracks printed at low scan speeds. With the variation in the scan speed, the amount of energy input into the material during printing varies. At a constant laser power, slower scan speeds result in higher heat input per unit length. When the scan speed reaches 600 mm/s, a transition to keyhole mode of melt pool is observed, which entails slower cooling rates during solidification; with an increase in the scan speed, the cooling rate also increases, and higher cooling rates as a result of relatively higher G and lower R , conditions with favour the formation of fine equiaxed grains, grains. However, printing at higher scan speeds also results in the formation of narrower tracks, which needs to be compensated by reducing the hatch distance in order to achieve full densification.

Bulk samples of the Ti-free material showed coarser grain sizes compared to its single-track counterparts. This is because that, in the absence of the inoculation in the Ti-free material, the remelting due to the track-by-track and layer-by-layer deposition

resulted in the epitaxial growth of columnar grains, which is typical in LB-PBF. However, for the SS441 and the Ti-high material, the grain sizes in bulk samples are finer compared to what is shown for all single tracks. This suggests that the remelting is beneficial for the inoculation as it provides sufficient time for the nucleation and growth of inoculant particles both in terms of their size and number density, resulting in the reduction in undercooling that is required for CET.

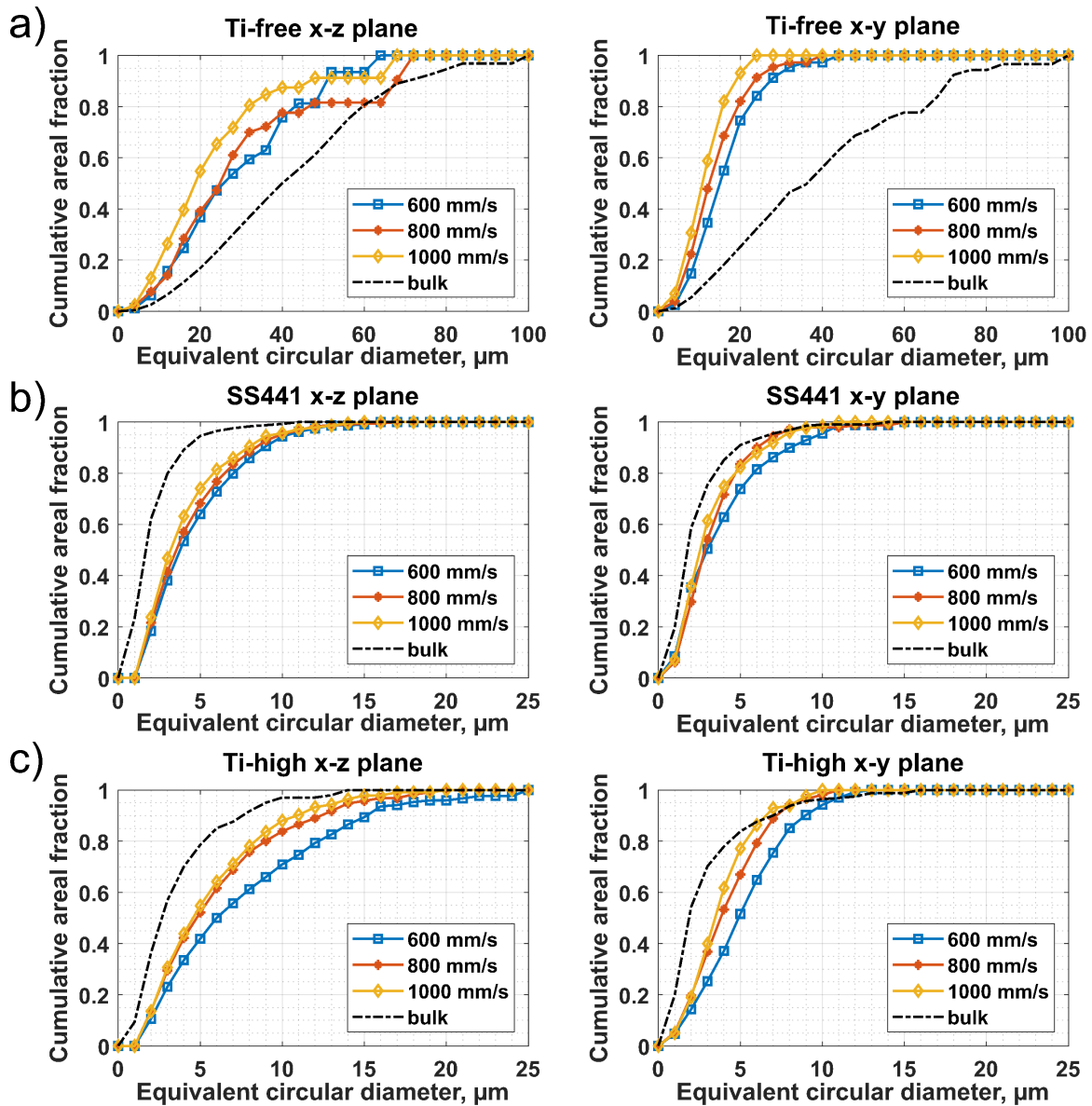


Figure 18 Distribution of grain size as a function of scan speeds for a) the Ti-free material, b) SS441 and c) the Ti-high material in single tracks, in comparison with the bulk samples of their respective materials.

6.3 Effect of nitrogen doping in the CoCrNi MEA

Influence of nitrogen on CoCrNi, with an aim to stabilize nitrogen as an interstitial element and its influence on the microstructure and room temperature mechanical properties was studied. Addition of nitrogen was observed to improve the densification behaviour with respect to processing parameter window and did not form any detrimental phase. Microstructural analysis revealed a cellular solidification structure (Figure 19a). Scheil solidification simulations predicted elemental segregation of chromium to cell walls in CoCrNi MEA (Figure 19c), and nitrogen along with chromium to the cell walls in the CoCrNi-N MEA (Figure 19b, d).

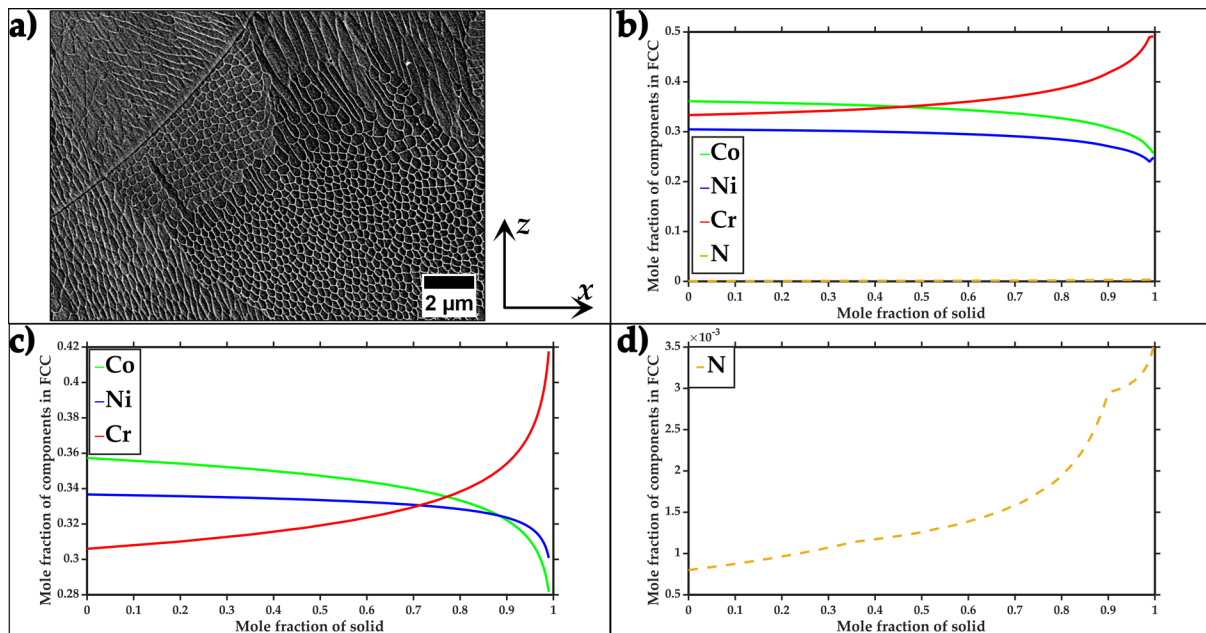


Figure 19 a) As-printed microstructure of CoCrNi-N MEA and Scheil solidification simulations showing elemental segregations for b) CoCrNi-N, c) CoCrNi and d) magnified inset for nitrogen segregation in CoCrNi-N.

In order to verify the stability of nitrogen as an interstitial, thermodynamic and kinetics calculations were performed to determine the formation kinetics of potential phases that could deplete nitrogen. The calculations predicted the rapid formation of Cr₂N between 800 and 1200 °C. As-printed samples were hence heat-treated for 30 minutes at different temperatures ranging between 800 and 1200 °C. The as-printed material did not show any presence of Cr₂N particles (Figure 20a). The formation of other types of particles/inclusions was observed mainly at the cell boundaries after

heat treatment at 800 °C (Figure 20 b). These particles were also observed to grow with increase in the heat treatment temperature and the samples heat treated at 1200 °C showed fully recrystallized microstructure with particles of different morphologies (Figure 20c). The EDS analysis of the particles revealed that all were chromium-rich oxides, and no nitrides were observed (Figure 20d). Hardness of the as-printed and heat-treated samples showed a difference of ~35 HV between CoCrNi-N and CoCrNi samples (Figure 20e). Based on the microstructural analysis and the hardness difference in as-printed and heat-treated samples, it can be inferred that nitrogen is stable as an interstitial element in the CoCrNi-N MEA.

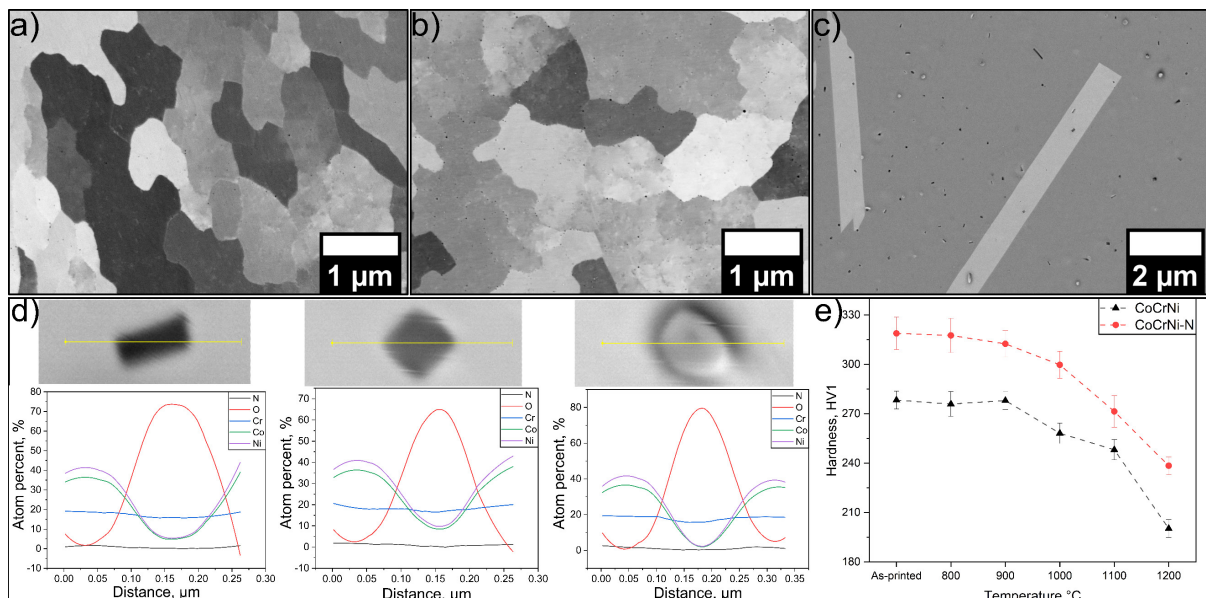


Figure 20 Back scattered electron images of CoCrNi-N samples in a) as-printed state, b) heat-treated at 800 °C c) heat treated at 1200 °C; d) EDS analysis of particles in the CoCrNi-N that was heat-treated at 1200 °C and e) hardness plots of as-printed and heat-treated samples of CoCrNi and CoCrNi-N MEAs.

Tensile tests performed on the as-printed samples of CoCrNi showed yield strength of 731 ± 6 MPa and ultimate tensile strength of 972 ± 7 MPa, while CoCrNi-N showed yield strength of 887 ± 10 MPa and ultimate tensile strength of 1109 ± 10 MPa. In both cases, minimum engineering strain of about 40% was reached. Overlapping the plastic regimes of the stress-strain curves for both materials indicate basically similar strain hardening response. The combination of yield and tensile strengths with high ductility

in both cases illustrates high toughness for the studied materials. The effect of nitrogen as an interstitial suggests an efficient solid solution strengthening effect.

Following conclusions are drawn from the work presented in this thesis.

In-situ inoculation in ferritic stainless steels

- Ferritic stainless steels pre-alloyed with titanium resulted in the formation of equiaxed grains with random $\langle 111 \rangle$ texture in the building direction, as compared to columnar grains with $\langle 100 \rangle$ texture in the Ti-free material, which indicates the change in the solidification conditions.
- EDS analysis showed the presence of aluminum-silicon containing oxides in Ti-free material which did not serve as inoculates as evident from the columnar grains. A mixture of pure titanium nitrides and core-shell structured oxy-nitrides were found in Ti-containing materials, which were effective in the inducing the inoculation.
- Single tracks experiments indicated the formation of finer grain sizes at higher scan speeds (1000 mm/s) in the Ti-free material. The bulk samples however consisted of much coarser grains compared to those in single tracks as a result of the epitaxial growth during the remelting by neighbouring tracks and subsequent layers.
- For both Ti-containing materials, fine, equiaxed grains with sizes under 1 μm are highly concentrated at the center of the melt pools, whereas slightly coarser, columnar grains were found at the periphery of the fine equiaxed grain zone. This is attributed to the favourable solidification conditions (relatively low G , high V , and long liquid lifetime) at the centers of the melt pools for the nucleation and growth of inoculants, which is also evidenced by the higher number density of titanium-nitride particles in the equiaxed grain regions.
- Single tracks in Ti-containing materials showed a similar trend as Ti-free materials with finer grain size observed in single tracks printed at higher scan

speeds. However, remelting as a result of the neighbouring tracks and layer by layer fabrication improved the grain refinement in the bulk samples.

LB-PBF of interstitial solid solution strengthened CoCrNi MEA

- As-printed microstructures revealed cellular solidification structure with elemental segregation of chromium and nitrogen to the cell walls, as predicted from Scheil solidification simulations.
- The as-printed CoCrNi showed yield strength of ~730 MPa and ultimate tensile strength of ~970 MPa, while CoCrNi-N showed yield strength of ~890 MPa and ultimate tensile strength of ~1110 MPa, revealing a clear influence of nitrogen as an interstitial solid solution strengthener.
- Nucleation of chromium-rich oxides was observed across the cell boundaries and remained there even upon heat treatments for both CoCrNi and CoCrNi-N. An increase in heat treatment temperature resulted in the coarsening of these oxides. Precipitation of Cr₂N was not observed. Recrystallized microstructure was observed after heat treatment at 1200 °C for both materials.
- CoCrNi-N exhibited almost a constant ~35 HV higher hardness, both in as-printed and heat-treated alloys, compared to that of CoCrNi.

The following aspects are not addressed yet in the current thesis but are considered to be done in the future.

Inoculation:

- To explore the influence of inoculation on the mechanical properties of the ferritic stainless steels.
- To explore the influence of ex-situ addition of inoculants on the CET in the columnar regions of both in-situ inoculated and inoculants-free ferritic stainless steels.
- To test the inoculation effect in austenitic steels or other FCC alloys that are manufactured using the LB-PBF process.

Medium entropy alloys:

- To study the thermal stability of the interstitial-MEAs manufactured using LB-PBF and its influence on the mechanical properties.
- To experimentally verify the cellular segregation of chromium in CoCrNi by compositional analysis.
- To understand the role of oxides on the microstructure development in CoCrNi.
- To understand the strengthening mechanisms (interstitial solid solution strengthening, grain boundary strengthening, precipitate strengthening and the TWIP effect) in the CoCrNi-N MEA
- To study the influence of the thermal stresses, induced by fast cooling rates during solidification in LB-PBF, on the possible martensitic transformations and the resultant microstructure and mechanical properties of quaternary MEAs.

Acknowledgements

I would like to thank both my supervisors Professor Lars Nyborg and Professor Sheng Guo for providing me with this opportunity and their guidance to work on some very interesting materials and processes. I would also like to thank them for very interesting discussions, encouragement, and support. I would like to express my gratitude to Professor Eduard Hryha for his encouragement and support. Special thanks to Dr. Zhuoer Chen for all the guidance and discussions.

I would also like to thank Associate Professor Greta Lindwall, Dr. Durga Ananthanarayanan, Dr. Niklas Holländer Pettersson for all the discussions over the last couple of years. I would like to thank Associate professor Fang Liu for all her support with the HRTEM and Professor Johan Ahlström for his help with the mechanical testing.

The industrial project partners Höganäs AB and Kanthal AB are acknowledged for their valuable input. Especially co-operation and contributions from Adjunct professors Karin Frisk and Sven Bengtsson, Höganäs AB and Mr. Roger Berglund, Kanthal AB, are acknowledged for materials supply, chemical analysis, and valuable discussions. I would also like to acknowledge Dr. Maheswaran Vattur Sundaram for his timely help.

I would like to offer my special thanks to Dr. Swathi K Manchili for her guidance, corrections, suggestions and for all kinds of support she provided after I moved to Sweden and for making the office more fun. Special thanks to Erika, Alberto, and Marcos for keeping me sane with all the games, trips, and fun especially during these tough times.

Thanks to all my friends and colleagues at the Department of Industrial and Materials Science, Fiona, William, Xiaolong, Daniel, Dimitri, Bharat, Angelica, Claudia, Dimitri, Camille, Antonio, Anok and Rasmus for creating a pleasant environment. I would like to take this opportunity to thank Dr. Ravi Bollina for always having my back and making this journey more fun. Last but not least, I would like to thank my parents, family, and friends back home and in Erlangen.

References

1. Bogue, R. 3D printing: the dawn of a new era in manufacturing? *Assembly Automation* **33**, 307–311 (2013).
2. Ngo, T. D., Kashani, A., Imbalzano, G., Nguyen, K. T. Q. & Hui, D. Additive manufacturing (3D printing): A review of materials, methods, applications and challenges. *Composites Part B: Engineering* **143**, 172–196 (2018).
3. Mao, M. *et al.* The emerging frontiers and applications of high-resolution 3D printing. *Micromachines* **8**, (2017).
4. 3D opportunity in aerospace and defense: Additive manufacturing takes flight | Deloitte Insights. <https://www2.deloitte.com/us/en/insights/focus/3d-opportunity/additive-manufacturing-3d-opportunity-in-aerospace.html>.
5. Kumar, L. J. & Krishnadas Nair, C. G. Current Trends of Additive Manufacturing in the Aerospace Industry. *Advances in 3D Printing and Additive Manufacturing Technologies* 39–54 (2017) doi:10.1007/978-981-10-0812-2_4.
6. Khajavi, S. H., Partanen, J. & Holmström, J. Additive manufacturing in the spare parts supply chain. *Computers in Industry* **65**, 50–63 (2014).
7. Yakout, M., Elbestawi, M. A. & Veldhuis, S. C. A Review of Metal Additive Manufacturing Technologies. (2018) doi:10.4028/www.scientific.net/SSP.278.1.
8. Additive manufacturing-Design-Part 1: Laser-based powder bed fusion of metals Fabrication additive-Conception-Partie 1: Fusion laser sur lit de poudre métallique COPYRIGHT PROTECTED DOCUMENT.
9. Herzog, D., Seyda, V., Wycisk, E. & Emmelmann, C. Additive manufacturing of metals. *Acta Materialia* **117**, 371–392 (2016).
10. AMPOWER Report on the Additive Manufacturing market. <https://additive-manufacturing-report.com/>.

11. Lewandowski, J. J. & Seifi, M. Metal Additive Manufacturing: A Review of Mechanical Properties. *Annual Review of Materials Research* **46**, 151–186 (2016).
12. Kou, S. *Welding metallurgy*. 666.
13. Yadroitsev, I., Bertrand, Ph., Antonenkova, G., Grigoriev, S. & Smurov, I. Use of track/layer morphology to develop functional parts by selective laser melting. *Journal of Laser Applications* **25**, 052003 (2013).
14. Spierings, A. B., Dawson, K., Uggowitz, P. J. & Wegener, K. Influence of SLM scan-speed on microstructure, precipitation of Al₃Sc particles and mechanical properties in Sc-and Zr-modified Al-Mg alloys.
15. Kusuma, C. The Effect of Laser Power and Scan Speed on Melt Pool Characteristics of Pure Titanium and Ti-6Al-4V Alloy for Selective Laser Melting. *Journal of Laser Applications* **25**, 052003 (2013).
16. Louw, D. F. & Pistorius, P. G. H. The effect of scan speed and hatch distance on prior-beta grain size in laser powder bed fused Ti-6Al-4V. *The International Journal of Advanced Manufacturing Technology* **103**:5, 2277–2286 (2019).
17. Scipioni Bertoli, U., Wolfer, A. J., Matthews, M. J., Delplanque, J. P. R. & Schoenung, J. M. On the limitations of Volumetric Energy Density as a design parameter for Selective Laser Melting. *Materials and Design* **113**, 331–340 (2017).
18. Ghosh, S. *et al.* Single-Track Melt-Pool Measurements and Microstructures in Inconel 625. *JOM* **70**:6, 1011–1016 (2018).
19. Monroy, K. P., Delgado, J., Sereno, L., Ciurana, J. & Hendrichs, N. J. Effects of the Selective Laser Melting manufacturing process on the properties of CoCrMo single tracks. *Metals and Materials International* **20**:5, 873–884 (2014).
20. Yadroitsev, I., Krakhmalev, P., Yadroitsava, I., Johansson, S. & Smurov, I. Energy input effect on morphology and microstructure of selective laser melting

- single track from metallic powder. *Journal of Materials Processing Technology* **213**, 606–613 (2013).
21. Yadroitsev, I. & Smurov, I. Selective laser melting technology: From the single laser melted track stability to 3D parts of complex shape. *Physics Procedia* **5**, 551–560 (2010).
 22. Jia, H., Sun, H., Wang, H., Wu, Y. & Wang, H. Scanning strategy in selective laser melting (SLM): a review. *The International Journal of Advanced Manufacturing Technology* 2021 113:9 **113**, 2413–2435 (2021).
 23. Marattukalam, J. J. *et al.* The effect of laser scanning strategies on texture, mechanical properties, and site-specific grain orientation in selective laser melted 316L SS. (2020) doi:10.1016/j.matdes.2020.108852.
 24. Dezfoli, A. R. A., Hwang, W.-S., Huang, W.-C. & Tsai, T.-W. Determination and controlling of grain structure of metals after laser incidence: Theoretical approach. *Scientific Reports* 2017 7:1 **7**, 1–11 (2017).
 25. Lee, Y., Nordin, M., Babu, S. S. & Farson, D. F. Effect of Fluid Convection on Dendrite Arm Spacing in Laser Deposition. *Metallurgical and Materials Transactions B* 2014 45:4 **45**, 1520–1529 (2014).
 26. Köhnen, P., Létang, M., Voshage, M., Schleifenbaum, J. H. & Haase, C. Understanding the process-microstructure correlations for tailoring the mechanical properties of L-PBF produced austenitic advanced high strength steel. *Additive Manufacturing* **30**, 100914 (2019).
 27. Zhang, X., Yocom, C. J., Mao, B. & Liao, Y. Microstructure evolution during selective laser melting of metallic materials: A review. *Journal of Laser Applications* **31**, 031201 (2019).
 28. Liu, X., Zhao, C., Zhou, X., Shen, Z. & Liu, W. Microstructure of selective laser melted AlSi10Mg alloy. *Materials & Design* **168**, 107677 (2019).

29. Yan, F., Xiong, W. & Faierson, E. J. Grain Structure Control of Additively Manufactured Metallic Materials. *Materials* 2017, Vol. 10, Page 1260 **10**, 1260 (2017).
30. Pham, M.-S., Dovggy, B., Hooper, P. A., Gourlay, C. M. & Piglione, A. The role of side-branching in microstructure development in laser powder-bed fusion. *Nature Communications* 2020 11:1 **11**, 1–12 (2020).
31. Murty, B. S., Kori, S. A. & Chakraborty, M. Grain refinement of aluminium and its alloys by heterogeneous nucleation and alloying. (2013)
doi:10.1179/095066001225001049.
32. Bermingham, M. J., StJohn, D. H., Krynen, J., Tedman-Jones, S. & Dargusch, M. S. Promoting the columnar to equiaxed transition and grain refinement of titanium alloys during additive manufacturing. *Acta Materialia* **168**, 261–274 (2019).
33. Yang, K. v., Shi, Y., Palm, F., Wu, X. & Rometsch, P. Columnar to equiaxed transition in Al-Mg(-Sc)-Zr alloys produced by selective laser melting. *Scripta Materialia* **145**, 113–117 (2018).
34. Greer, A. L., Perepezko, J. H., Franks, F., Cantor, B. & Cahn, R. W. Grain refinement of alloys by inoculation of melts. in *Philosophical Transactions of the Royal Society A: Mathematical, Physical and Engineering Sciences* vol. 361 479–495 (Royal Society, 2003).
35. Wallace, J. F. Grain Refinement of Steels. *Jom* **15**, 372–376 (1963).
36. Greer, A. L. & Quedsted, T. E. Heterogeneous grain initiation in solidification. <https://doi.org/10.1080/14786430500198486> **86**, 3665–3680 (2007).
37. Martin, J. H. *et al.* 3D printing of high-strength aluminium alloys. *Nature* 2017 549:7672 **549**, 365–369 (2017).

38. Martin, J. H. *et al.* Grain refinement mechanisms in additively manufactured nano-functionalized aluminum. *Acta Materialia* **200**, 1022–1037 (2020).
39. Fredriksson, Hasse. & Akerlind, Ulla. Solidification and Crystallization Processing in Metals and Alloys. 828 (2012).
40. Kennedy, J. R. *et al.* The potential for grain refinement of Wire-Arc Additive Manufactured (WAAM) Ti-6Al-4V by ZrN and TiN inoculation. *Additive Manufacturing* **40**, 101928 (2021).
41. Mereddy, S. *et al.* Trace Carbon Addition to Refine Microstructure and Enhance Properties of Additive-Manufactured Ti-6Al-4V. *JOM* 2018 70:9 **70**, 1670–1676 (2018).
42. Rolchigo, M. R. *et al.* Modeling of Ti-W Solidification Microstructures Under Additive Manufacturing Conditions. *Metallurgical and Materials Transactions A* 2017 48:7 **48**, 3606–3622 (2017).
43. Bermingham, M. J., McDonald, S. D., Buddery, A. J., Stjohn, D. H. & Dargusch, M. S. Processing considerations for cast Ti-25Nb-3Mo-3Zr-2Sn biomedical alloys. *Materials Science and Engineering: C* **31**, 1520–1525 (2011).
44. Zhang, D. *et al.* Grain Refinement of Alloys in Fusion-Based Additive Manufacturing Processes. *Metallurgical and Materials Transactions A* 2020 51:9 **51**, 4341–4359 (2020).
45. Belelli, F., Casati, R., Larini, F., Riccio, M. & Vedani, M. Investigation on two Ti-B-reinforced Al alloys for Laser Powder Bed Fusion. *Materials Science and Engineering: A* **808**, 140944 (2021).
46. Li, X. P. *et al.* Selective laser melting of nano-TiB₂ decorated AlSi10Mg alloy with high fracture strength and ductility. *Acta Materialia* **129**, 183–193 (2017).

47. Thapliyal, S. *et al.* Design of heterogeneous structured Al alloys with wide processing window for laser-powder bed fusion additive manufacturing. *Additive Manufacturing* **42**, 102002 (2021).
48. Li, B., Qian, B., Xu, Y., Liu, Z. & Xuan, F. Fine-structured CoCrFeNiMn high-entropy alloy matrix composite with 12 wt% TiN particle reinforcements via selective laser melting assisted additive manufacturing. *Materials Letters* **252**, 88–91 (2019).
49. Ikehata, H. & Jäggle, E. Grain refinement of Fe-X alloys fabricated by laser powder bed fusion. *Materials Science Forum* **1016 MSF**, 580–586 (2021).
50. Ikehata, H. & Jäggle, E. Evaluation of microstructure and tensile properties of grain-refined, Ti-alloyed ferritic stainless steel fabricated by laser powder bed fusion. *Materials Science and Engineering: A* **818**, 141365 (2021).
51. Karlsson, D. *et al.* Additive manufacturing of the ferritic stainless steel SS441. *Additive Manufacturing* **36**, 101580 (2020).
52. Bramfitt, B. L. The effect of carbide and nitride additions on the heterogeneous nucleation behavior of liquid iron. *Metallurgical Transactions* **1**, 2958 (1970).
53. Durga, A. *et al.* Grain refinement in additively manufactured ferritic stainless steel by in situ inoculation using pre-alloyed powder. *Scripta Materialia* **194**, (2021).
54. Liverani, E., Toschi, S., Ceschini, L. & Fortunato, A. Effect of selective laser melting (SLM) process parameters on microstructure and mechanical properties of 316L austenitic stainless steel. *Journal of Materials Processing Technology* **249**, 255–263 (2017).
55. Liu, S. & Shin, Y. C. Additive manufacturing of Ti6Al4V alloy: A review. *Materials & Design* **164**, 107552 (2019).

56. Mertens, A. I., Delahaye, J. & Lecomte-Beckers, J. Fusion-Based Additive Manufacturing for Processing Aluminum Alloys: State-of-the-Art and Challenges. *Advanced Engineering Materials* **19**, 1700003 (2017).
57. Gong, X. & Chou, K. Microstructures of Inconel 718 by Selective Laser Melting. *TMS 2015 144th Annual Meeting & Exhibition* 461–468 (2015) doi:10.1007/978-3-319-48127-2_58.
58. Hu, Y., Mao, W., Yan, P. & Li, N. Effect of Normalizing Treatment on Mechanical Properties of AISI 441 Stainless Steel Prepared by Investment Casting. *Metals* **2021**, Vol. 11, Page 474 **11**, 474 (2021).
59. Sello, M. P. & Stumpf, W. E. Laves phase precipitation and its transformation kinetics in the ferritic stainless steel type AISI 441. *Materials Science and Engineering: A* **528**, 1840–1847 (2011).
60. Sello, M. P. & Stumpf, W. E. Laves phase embrittlement of the ferritic stainless steel type AISI 441. *Materials Science and Engineering: A* **527**, 5194–5202 (2010).
61. Yang, Z. *et al.* Investigation of AISI 441 Ferritic Stainless Steel and Development of Spinel Coatings for SOFC Interconnect Applications. <http://www.ntis.gov/ordering.htm> (2008).
62. Maruma, M. G., Siyasiya, C. W. & Stumpf, W. E. Mount Grace Country House and Spa, Magaliesburg, South Africa.. 115 *The Journal of The Southern African Institute of Mining and Metallurgy*. **113**, 15–17 (2013).
63. Cantor, B., Chang, I. T. H., Knight, P. & Vincent, A. J. B. Microstructural development in equiatomic multicomponent alloys. *Materials Science and Engineering: A* **375–377**, 213–218 (2004).
64. Yeh, J. W. *et al.* Nanostructured high-entropy alloys with multiple principal elements: Novel alloy design concepts and outcomes. *Advanced Engineering Materials* **6**, 299–303 (2004).

65. Li, Z., Zhao, S., Ritchie, R. O. & Meyers, M. A. Mechanical properties of high-entropy alloys with emphasis on face-centered cubic alloys. *Progress in Materials Science* **102**, 296–345 (2019).
66. George, E. P., Raabe, D. & Ritchie, R. O. High-entropy alloys. *Nature Reviews Materials* 2019 4:8 **4**, 515–534 (2019).
67. Miracle, D. B. High entropy alloys as a bold step forward in alloy development. *Nature Communications* **10**, 1–3 (2019).
68. Tsai, M. H. & Yeh, J. W. High-entropy alloys: A critical review. *Materials Research Letters* **2**, 107–123 (2014).
69. Zhou, Y. *et al.* Design of non-equiatomic medium-entropy alloys. *Scientific Reports* 2018 8:1 **8**, 1–9 (2018).
70. Jiang, L. *et al.* Effect of Mo and Ni elements on microstructure evolution and mechanical properties of the CoFeNi_xVMoy high entropy alloys. *Journal of Alloys and Compounds* **649**, 585–590 (2015).
71. Singh, S., Wanderka, N., Murty, B. S., Glatzel, U. & Banhart, J. Decomposition in multi-component AlCoCrCuFeNi high-entropy alloy. *Acta Materialia* **59**, 182–190 (2011).
72. Manzoni, A., Daoud, H., Völkl, R., Glatzel, U. & Wanderka, N. Phase separation in equiatomic AlCoCrFeNi high-entropy alloy. *Ultramicroscopy* **132**, 212–215 (2013).
73. Cheng, C. Y. & Yeh, J. W. High thermal stability of the amorphous structure of GexNbTaTiZr (x=0.5, 1) high-entropy alloys. *Materials Letters* **181**, 223–226 (2016).
74. Zhang, Y., Zhou, Y. J., Lin, J. P., Chen, G. L. & Liaw, P. K. Solid-Solution Phase Formation Rules for Multi-component Alloys. *Advanced Engineering Materials* **10**, 534–538 (2008).

75. Guo, S., Ng, C., Lu, J. & Liu, C. T. Effect of valence electron concentration on stability of fcc or bcc phase in high entropy alloys. *Journal of Applied Physics* **109**, 103505 (2011).
76. Yeh, J.-W. Physical Metallurgy of High-Entropy Alloys. *JOM* *2015* **67:10** **67**, 2254–2261 (2015).
77. Guo, S. & Liu, C. T. Phase stability in high entropy alloys: Formation of solid-solution phase or amorphous phase. *Progress in Natural Science: Materials International* **21**, 433–446 (2011).
78. Guo, S. Phase selection rules for cast high entropy alloys: an overview. <https://doi.org/10.1179/1743284715Y.0000000018> **31**, 1223–1230 (2015).
79. Singh, A. K., Kumar, N., Dwivedi, A. & Subramaniam, A. A geometrical parameter for the formation of disordered solid solutions in multi-component alloys. *Intermetallics* **53**, 112–119 (2014).
80. Yang, X. & Zhang, Y. Prediction of high-entropy stabilized solid-solution in multi-component alloys. *Materials Chemistry and Physics* **132**, 233–238 (2012).
81. Huang, H. *et al.* Strengthening CoCrNi medium-entropy alloy by tuning lattice defects. *Scripta Materialia* **188**, 216–221 (2020).
82. Liu, J. P. *et al.* Superior strength-ductility CoCrNi medium-entropy alloy wire. *Scripta Materialia* **181**, 19–24 (2020).
83. Huang, H. *et al.* Strengthening CoCrNi medium-entropy alloy by tuning lattice defects. *Scripta Materialia* **188**, 216–221 (2020).
84. Li, Z., Pradeep, K. G., Deng, Y., Raabe, D. & Tasan, C. C. Metastable high-entropy dual-phase alloys overcome the strength-ductility trade-off. *Nature* **534**, 227–30 (2016).
85. Gludovatz, B. *et al.* Exceptional damage-tolerance of a medium-entropy alloy CrCoNi at cryogenic temperatures. *Nature Communications* **7**, 1–8 (2016).

86. Soundararajan, C. K., Luo, H., Raabe, D. & Li, Z. Hydrogen resistance of a 1 GPa strong equiatomic CoCrNi medium entropy alloy. *Corrosion Science* **167**, 108510 (2020).
87. Weng, F. *et al.* Influence of oxides on the cryogenic tensile properties of the laser aided additive manufactured CoCrNi medium entropy alloy. *Composites Part B: Engineering* **216**, 108837 (2021).
88. Adomako, N. K., Kim, J. H. & Hyun, Y. T. High-temperature oxidation behaviour of low-entropy alloy to medium- and high-entropy alloys. *Journal of Thermal Analysis and Calorimetry* *2018* **133:1** **133**, 13–26 (2018).
89. Shang, X. *et al.* The intrinsic mechanism of corrosion resistance for FCC high entropy alloys. *Science China Technological Sciences* *2017* **61:2** **61**, 189–196 (2017).
90. Moravcik, I. *et al.* Yield strength increase of a CoCrNi medium entropy alloy by interstitial nitrogen doping at maintained ductility. *Scripta Materialia* **178**, 391–397 (2020).
91. Niu, P. *et al.* Microstructure, Properties, and Metallurgical Defects of an Equimolar CoCrNi Medium Entropy Alloy Additively Manufactured by Selective Laser Melting. *Metallurgical and Materials Transactions A* *2021* **52:2** **52**, 753–766 (2021).
92. Moravcik, I. *et al.* Nitrogen interstitial alloying of CoCrFeMnNi high entropy alloy through reactive powder milling. *Entropy* **21**, 1–7 (2019).
93. Moravcik, I. *et al.* Interstitial doping enhances the strength-ductility synergy in a CoCrNi medium entropy alloy. *Materials Science and Engineering: A* **781**, 139242 (2020).
94. Moravcik, I. *et al.* Interstitial nitrogen enhances corrosion resistance of an equiatomic CoCrNi medium-entropy alloy in sulfuric acid solution. *Materials Characterization* **172**, 110869 (2021).

95. Schindelin, J. *et al.* Fiji: an open-source platform for biological-image analysis. *Nature Methods* 2012 9:7 **9**, 676–682 (2012).
96. Goodhew, P. J., Humphreys, J. & Humphreys, J. Electron Microscopy and Analysis. *Electron Microscopy and Analysis* (2000) doi:10.1201/9781482289343.
97. Ponor. Electron-matter interaction volume and various types of signal generated - Wikimedia Commons.
<https://commons.wikimedia.org/w/index.php?curid=93635964>.
98. Bachmann, F., Hielscher, R. & Schaeben, H. Texture Analysis with MTEX – Free and Open Source Software Toolbox. *Solid State Phenomena* **160**, 63–68 (2010).
99. Jeffery, G. A. Elements of x-ray diffraction (Cullity, B. D.). *Journal of Chemical Education* **34**, A178 (1957).
100. Andersson, J. O., Helander, T., Höglund, L., Shi, P. & Sundman, B. Thermo-Calc & DICTRA, computational tools for materials science. *Calphad* **26**, 273–312 (2002).
101. Fu, J., Nie, Q., Qiu, W., Liu, J. & Wu, Y. Morphology, orientation relationships and formation mechanism of TiN in Fe-17Cr steel during solidification. *Materials Characterization* **133**, 176–184 (2017).
102. Hunter, A. & Ferry, M. Texture enhancement by inoculation during casting of ferritic stainless steel strip. *Metallurgical and Materials Transactions A: Physical Metallurgy and Materials Science* **33**, 1499–1507 (2002).

